

The correlated insulators of magic angle twisted bilayer graphene at zero and one quantum of magnetic flux: a tight-binding study

Miguel Sánchez Sánchez* and Tobias Stauber†
Instituto de Ciencia de Materiales de Madrid CSIC, Madrid (Spain)

Magic angle twisted bilayer graphene (MATBG) has become one of the prominent topics in Condensed Matter during the last few years, however, fully atomistic studies of the interacting physics are missing. In this work, we study the correlated insulator states of MATBG in the setting of a tight-binding model, under a perpendicular magnetic field of 0 and 26.5 T, corresponding to zero and one quantum of magnetic flux per unit cell. At zero field and for dopings of two holes ($\nu = -2$) or two electrons ($\nu = +2$) per unit cell, the Kramers intervalley coherent (KIVC) order is the ground state at the Hartree-Fock level, although it is stabilized by a different mechanism to that in continuum model. At charge neutrality, the spin polarized state is competitive with the KIVC due to the on-site Hubbard energy. We obtain a strongly electron-hole asymmetric phase diagram with robust insulators for electron filling and metals for negative filling. In the presence of magnetic flux, we predict an insulator with Chern number -2 for $\nu = -2$, a spin polarized state at charge neutrality and competing insulators with Chern numbers $+2$ and 0 at $\nu = +2$. The stability of the $\nu = +2$ insulators is determined by the screening environment, allowing for the possibility of observing a topological phase transition.

I. INTRODUCTION

Magic angle twisted bilayer graphene (MATBG) is a two dimensional quantum material[1] that exhibits a plethora of exotic phases ranging from superconductors[2–5] to strange metals[6, 7], passing through integer[8, 9] and fractional[10] Chern Insulators. It constitutes a remarkable platform for the understanding of the many-body problem in Condensed Matter and the interplay of strong interactions and topology[11–13], and inaugurated the field of moiré materials[14–17].

The correlated insulators arise when the doping level is such that the number of electrons per unit cell is an integer number. They were discovered before the superconductivity and other phases[18], and are one of the most studied phenomena in twisted bilayer graphene (TBG)[3–5, 8, 9, 18–43].

On another hand, crystalline systems under magnetic fields are controlled by the scale given by the magnetic flux quantum $\Phi_0 = h/e$ [44, 45]. When the magnetic field is such that the flux per unit cell is comparable to Φ_0 , the system is in the 'Hofstadter regime' and the picture of Landau levels is replaced by a reentrant band structure[46, 47]. In typical materials such magnetic fields are of the order of 10^4 T, but in MATBG the large moiré unit cell allows accessible fields of the order of 30 T. In MATBG the Landau level spectrum of the correlated insulators has been studied[3, 4, 8, 9, 48, 49]. Also, at one magnetic flux quantum reentrant correlated insulators have been predicted and observed[50–52].

On the theory side, the Bistritzer-McDonald (BM) or continuum model[53, 54] is a low energy theory that has proven very powerful in understanding the physics of

TBG, revealing the emergent symmetries of the system that have led to the picture of the 'U(4) ferromagnets' for the correlated insulators[19, 20, 32–35, 37]. However, the model, with only a handful of parameters, cannot capture the finer details of the spectrum and the wave functions. These differences at low energy scales are relevant in the competition between states.

In this work we employ a tight-binding model for MATBG. The high computational cost, which makes atomistic studies scarce in this system[27–29, 55], is partially bypassed by a projection onto the subspace of the low energy bands (the 'flat bands'). The external magnetic flux is tuned to zero and one magnetic flux quantum per unit cell, we focus on samples without strain and leave electron-phonon coupling for future work.

The explicit breaking of the $U(4)$ symmetry of MATBG is assessed via the particle-hole asymmetry of the flat bands[56], the intervalley Hund's coupling[21] and the on-site Hubbard interaction. We find that the intervalley Hund's coupling, relevant for the superconductivity, has antiferromagnetic contributions due to the long range Coulomb interaction. On the other hand, the Hubbard term contributes to a ferromagnetic coupling.

To study the spontaneous symmetry breaking in the correlated states, we perform self-consistent Hartree-Fock simulations. For $\Phi = 0$ we find agreement with previous results on the nature of the ground state at even filling[20–22, 32, 34, 36], but the selection mechanism of the ground state is different. Instead of kinetic energy superexchange as expected in the BM model, the appearance of 'inter-Chern' order near the Γ point reduces the exchange energy and stabilizes the Kramers intervalley coherent state. In addition, the Hubbard interaction makes the spin polarized state competitive at charge neutrality. The self-consistent states are insulating at electron doping and metallic at hole doping, signalling the experimentally reported many-body electron-hole asymmetry[3, 4, 38].

* miguel.sanchez@csic.es

† tobias.stauber@csic.es

For $\Phi = \Phi_0$, the system departs from the strong coupling $U(4)$ picture due to the increased bandwidth of the kinetic energy bands, in the same manner as the strained samples at zero flux[22, 39]. Consistently for different screening environments, we observe an insulator with Chern number -2 at $\nu = -2$ and a spin polarized state at $\nu = 0$. For $\nu = +2$ we observe a topological phase transition from an insulator with Chern number $+2$ for small screening to an intervalley coherent trivial insulator for large screening. The Chern $+2$ insulator is compatible with the experimental data of Ref. [52].

The paper is organized as follows. In section II we describe the tight-binding model of TBG and the Peierls' substitution under magnetic field, in section III we introduce the emergent $U(4)$ symmetry at the magic angle and in section IV we discuss the explicit breaking of $U(4)$ in the lattice model. Finally, in section V we report the correlated states obtained in the Hartree-Fock simulations, and in section VI we draw some conclusions.

II. THE MODEL

In graphene, the primitive vectors are $\mathbf{a}_1 = a(1/2, \sqrt{3}/2)$ and $\mathbf{a}_2 = a(-1/2, \sqrt{3}/2)$, with $a = \sqrt{3}a_0$ and $a_0 = 0.142$ nm the carbon-carbon distance. Atoms at lattice points belong to sublattice A , and their nearest neighbours displaced by $(\mathbf{a}_1 + \mathbf{a}_2)/3$ to sublattice B .

Consider two graphene layers stacked on top of each other, at $z = -d_0/2$ and $z = d_0/2$ respectively, being $d_0 = 0.335$ nm the interlayer distance, such that top and bottom atoms are vertically aligned. The bottom layer is rotated by an angle $-\theta/2$, and the top layer by $\theta/2$, with the center of rotation being the center of one of the graphene hexagons. We choose a value of θ that makes the twisted structure commensurate[54]. In our case, we parametrize the angle by an integer n_θ such that $\cos(\theta) = 1 - 1/2(3n_\theta^2 + 3n_\theta + 1)$. The unit vectors of the superlattice are

$$\begin{aligned} \mathbf{L}_1 &= R_{-\theta/2}(n_\theta \mathbf{a}_1 + (n_\theta + 1)\mathbf{a}_2) = L_M(0, 1), \\ \mathbf{L}_2 &= R_{\pi/3} \mathbf{L}_1 = R_{-\theta/2}((-n_\theta - 1)\mathbf{a}_1 + (2n_\theta + 1)\mathbf{a}_2), \end{aligned} \quad (1)$$

with R_α a rotation by angle α and L_M the lattice constant. The reciprocal vectors are given by

$$\begin{aligned} a_0 \mathbf{G}_1 &= G_\theta R_{-\theta/2}((3n_\theta + 1)\mathbf{a}_1 + \mathbf{a}_2), \\ a_0 \mathbf{G}_2 &= R_{-2\pi/3}(\mathbf{G}_1) \\ &= G_\theta R_{-\theta/2}(-(3n_\theta + 2)\mathbf{a}_1 + (3n_\theta + 1)\mathbf{a}_2), \end{aligned} \quad (2)$$

where $G_\theta = \frac{4\pi}{3a_0}(9n_\theta^2 + 9n_\theta + 3)^{-1}$. The magic angle is approximately given by $n_\theta = 31$ (1.05°), corresponding to a Moiré lattice constant of $L_M = 13.4$ nm and 11908 atoms in the unit cell.

The point group of this structure is the dihedral group D_6 , generated by six-fold rotations around the z axis,

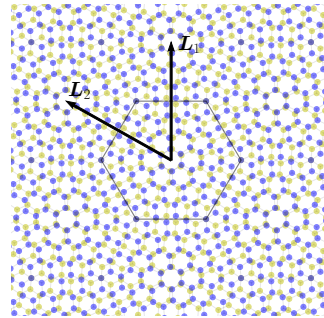


FIG. 1: **Top view of twisted bilayer graphene** for a twist angle of $\theta = 9.43^\circ$. The hexagonal Wigner-Seitz cell is indicated. The center of the unit cell is locally AA stacked (the two layers are on top of each other), and the corners are AB, or BA stacked (only A atoms are on top of B atoms, or *vice versa*).

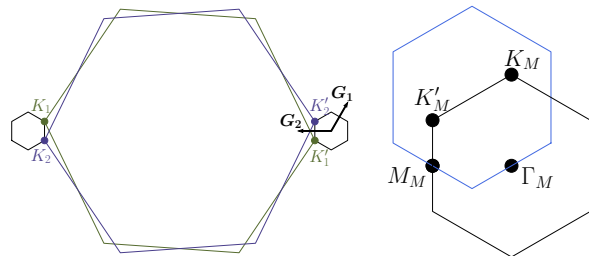


FIG. 2: **Brillouin zone of MATBG**. **Left:** Brillouin zone of the decoupled monolayers in purple and green, and Moiré Brillouin zone of TBG in black. Low energy TBG states belong to valley K or K' of each monolayer. The interlayer tunneling couples both graphene sheets, with negligible mixing between valleys. **Right:** Redefined high-symmetry momenta at one magnetic flux quantum in the periodic Landau gauge. The BZ gets shifted by $(\mathbf{G}_1 + \mathbf{G}_2)/2$ (see Appendix A).

C_{6z} , and two-fold rotations around the y axis, C_{2y} , leaving the origin fixed. The combined operation $C_{6z}^3 = C_{2z}$ amounts to a two-fold rotation around the z axis, and $C_{2x} = C_{2y}C_{2z} = C_{2x}$ to a two-fold rotation around the x axis. The spin-orbit coupling being small, spinless time-reversal \mathcal{T} is also a symmetry.

Lattice relaxation is included via in-plane distortions following the model of Ref.[57]. The effect of relaxation is to enlarge the AB and BA regions and reduce the AA regions of the Moiré pattern (see Fig. 1), preserving all the crystallographic symmetries.

We employ the Slater-Koster parametrization of the hopping integral of Ref.[58], with a p_z orbital per carbon atom and spin, giving the Hamiltonian

$$H_0 = \sum_{\mathbf{r}_i, \mathbf{r}_j, s} t(\mathbf{r}_i - \mathbf{r}_j) c_{i,s}^\dagger c_{j,s}, \quad (3)$$

$c_{i,s}^\dagger$ being the creation operator of an electron with spin s

at position \mathbf{r}_i . The hopping integral is decomposed into σ and π -bond hoppings,

$$t(\mathbf{r}) = -V_{pp\pi}(r) \left(1 - \left(\frac{\mathbf{r} \cdot \hat{\mathbf{z}}}{r} \right)^2 \right) + V_{pp\sigma}(r) \left(\frac{\mathbf{r} \cdot \hat{\mathbf{z}}}{r} \right)^2,$$

$$V_{pp\pi}(r) = V_{pp\pi}^0 e^{-(r-a_0)/r_0},$$

$$V_{pp\sigma}(r) = V_{pp\sigma}^0 e^{-(r-d_0)/r_0}, \quad (4)$$

with the parameters $V_{pp\pi}^0 = 2.7$ eV, $V_{pp\sigma}^0 = 0.48$ eV and $r_0 = 0.0453$ nm.

The Coulomb interaction is implemented by the double-gated potential

$$V = \frac{1}{2} \sum_{\mathbf{r}_i, \mathbf{r}_j, s_i, s_j} V(\mathbf{r}_i - \mathbf{r}_j) : c_{i, s_i}^\dagger c_{i, s_i} c_{j, s_j}^\dagger c_{j, s_j} :,$$

$$V(\mathbf{r}_i - \mathbf{r}_j) = \frac{e^2}{4\pi\epsilon_0\epsilon} \sum_n \frac{(-1)^n}{\|\mathbf{r}_i - \mathbf{r}_j + n\xi\hat{\mathbf{z}}\|}, \quad (5)$$

which applies for the experimental setups where two metallic plates are placed at $z = \pm\xi/2$. Unless stated otherwise, we set $\xi = 10$ nm. The dielectric constant ϵ accounts for the screening due to the substrate and internal screening due to the electrons. The interaction is normal ordered[59] with respect to the ground state of two decoupled graphene layers at charge neutrality. This choice of normal ordering is also called graphene subtraction scheme[30, 31]. Under magnetic field, we do not include the Zeeman shift when calculating the graphene state, so that the spin imbalances come entirely from the flat band physics. The on-site Hubbard term is also considered

$$H_U = U \sum_{\mathbf{r}_i} : c_{i\uparrow}^\dagger c_{i\uparrow} c_{i\downarrow}^\dagger c_{i\downarrow} :. \quad (6)$$

The total Hamiltonian is then $H = H_0 + V + H_U$.

Minimal coupling to an external magnetic field

At nonzero magnetic field, the Peierls' substitution[60] adds a phase to the hopping elements,

$$t(\mathbf{r}_i - \mathbf{r}_j) \rightarrow t(\mathbf{r}_i - \mathbf{r}_j) e^{i\theta_{i,j}},$$

$$\theta_{i,j} = \frac{2\pi}{\Phi_0} \int_{\mathbf{r}_i \rightarrow \mathbf{r}_j} \mathbf{A}(\mathbf{r}') \cdot d\mathbf{r}', \quad (7)$$

where $\Phi_0 = h/e$ is the quantum of magnetic flux, and the line integral goes from \mathbf{r}_i to \mathbf{r}_j in a straight line if the orbitals are well localized[46].

In the presence of magnetic flux, the translation operators pick up an Aharonov-Bohm phase. They act on the single-particle states as[45]

$$\tilde{T}_1 = \sum_{\mathbf{r}_i} e^{-2\pi i \xi_2 \phi - i\theta_{i, i+\mathbf{L}_1}} c_{i+\mathbf{L}_1}^\dagger c_i,$$

$$\tilde{T}_2 = \sum_{\mathbf{r}_i} e^{2\pi i \xi_1 \phi - i\theta_{i, i+\mathbf{L}_2}} c_{i+\mathbf{L}_2}^\dagger c_i. \quad (8)$$

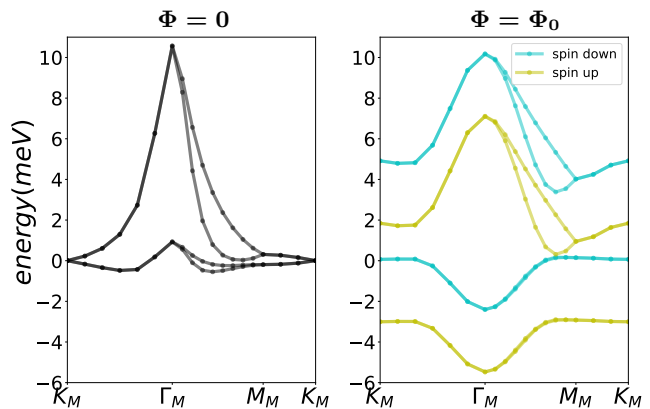


FIG. 3: **Band structure of MATBG ($\theta = 1.05^\circ$)** along the high symmetry $K_M \Gamma_M M_M K_M$ line. **Left:** flat bands at zero field. **Right:** flat bands at $B = 26.5$ T. The Zeeman energy produces a splitting of ~ 3 meV.

ξ_{i1} and ξ_{i2} are defined by $\mathbf{r}_i = \xi_{i1} \mathbf{L}_1 + \xi_{i2} \mathbf{L}_2$, and $\phi = \Phi/\Phi_0 = BA_M/\Phi_0$ is the flux per moiré unit cell in units of Φ_0 .

It can be shown that $[\mathcal{H}, \tilde{T}_1] = [\mathcal{H}, \tilde{T}_2] = 0$ and $\tilde{T}_1 \tilde{T}_2 = e^{-2\pi i \phi} \tilde{T}_2 \tilde{T}_1$, so the translational symmetries are broken in general. However, if ϕ is a rational number p/q one can choose the set of commuting operators $\{\tilde{T}_1, \tilde{T}_2^q\}$, or $\{\tilde{T}_1^q, \tilde{T}_2\}$ and diagonalize them simultaneously with the Hamiltonian. Translational symmetry is then recovered at rational fluxes with a unit cell that is q times larger than at zero flux, and the Bloch waves are generalized to magnetic waves having good \tilde{T}_1 and \tilde{T}_2^q quantum numbers.

In the periodic Landau gauge[61]

$$\mathbf{A}(\mathbf{r}) = \frac{\Phi}{2\pi} \left(\xi_1 \mathbf{G}_2 - 2\pi \nabla (\xi_2 [\xi_1 + \epsilon]) \right)$$

$$= \frac{\Phi}{2\pi} \left(-\xi_2 \sum_n \delta(\xi_1 - n + \epsilon) \mathbf{G}_1 + (\xi_1 - [\xi_1 + \epsilon]) \mathbf{G}_2 \right), \quad (9)$$

the phases of the translation operators $\tilde{T}_2^q, \tilde{T}_1$ cancel and the Bloch waves have the same form as in zero flux ($\lfloor \dots \rfloor$ is the floor function). The infinitesimal ϵ prevents ambiguities if some atoms lie at integer values of ξ_1 . The momentum \mathbf{k} takes the possible values in the magnetic Brillouin zone of the dual lattice with lattice vectors \mathbf{G}_1 and \mathbf{G}_2/q . Under magnetic flux, time reversal \mathcal{T} and rotations C_{2y}, C_{2x} reverse the sign of the external field, but the rotations around the z axis are preserved[62].

Besides orbital effects, the Zeeman energy $-g\mu_B B s_z/\hbar$ ($g = 2$ is the gyromagnetic ratio of the electron and μ_B the Bohr magneton) is also taken into account. For 26.5 T it amounts to ± 1.535 meV.

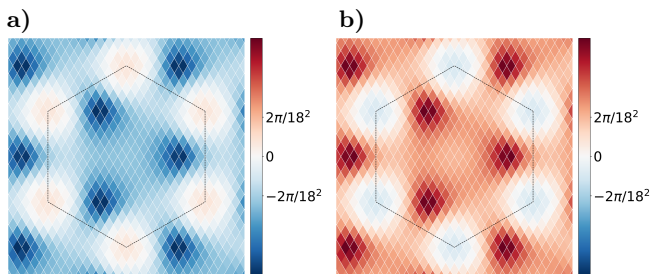


FIG. 4: **Integrated Berry curvature at $B = 26.5$**

T. We calculate the integrated Berry curvature on a 18×18 grid. **a)** Valley K valence band (Chern number -1). **b)** Valley K conduction band (Chern number $+1$).

C_{2z} symmetry interchanges the conduction/valence bands (see the text for the definition of the valley charge).

Results of the non interacting model

In Fig. 3 we plot the spectrum of MATBG for $n_\theta = 31$. At the charge neutrality point there are 8 quasi flat bands (2 layers \times 2 valleys \times 2 spin polarizations) with a bandwidth of around 10 meV and well separated from the 'remote' bands. The filling is parametrized by $\nu \in (-4, 4)$, being $\nu = 0$ the neutrality point and $\nu = +4$ (-4) the filled (empty) flat bands. When the external magnetic field is 26.5 T, we have $\Phi = \Phi_0$ and the flat bands are reentrant. The symmetry $C_{2z}\mathcal{T}$ that preserves the gapless Dirac points in zero flux[63] is broken, and the Dirac cones are gapped with a Chern number of -2 [47]. In the flat bands the kinetic energy is small and the interacting physics dominates, giving rise to the rich phase diagram of MATBG.

In Fig. 4 we plot the Berry curvatures of the bands at 26.5 T. In the discretized Brillouin zone, we compute the integrated Berry curvature on the parallelograms defined by the discretization, following Ref. [64]. We see an emergent symmetry relating the Berry curvatures of valence and conduction bands.

III. THE $U(4)$ SYMMETRY

A starting point for the understanding the physics of MATBG is the projected limit, in which the Fermi sea of the remote bands is 'frozen' and the scattering is restricted to states within the flat bands. The correlated insulators are 'generalized ferromagnets' that spontaneously break a $U(4)$ (or a larger $U(4) \times U(4)$) global symmetry. For a detailed discussion on this symmetry, we refer the reader to Refs. [12, 21, 33, 50]. Here, we describe the most 'physical' subgroups. The full group is generated from these.

- $U(1)_v$. The non interacting eigenstates belong to valley K (valley charge $+1$) or K' (valley charge -1) of each of the graphene monolayers, see Fig.

2. Charge non conserving terms of the screened Coulomb interaction are suppressed, hence $U(1)_v$ is a symmetry of the interacting system. We write $\eta = +1(-1)$ for valley $K(K')$. The valley charge operator is denoted by τ_z , with eigenvalues $\langle \tau_z \rangle = \eta$. Electric charge $U(1)_c$ is also a symmetry.

- $SU(2)_K \times SU(2)_{K'}$. The exchange integral of pairs of states with different valley charges is suppressed due to the big momentum transfer, and only the Hartree term contributes to the energy. This implies a symmetry of independent spin rotations in each valley, which do not change the total density. At nonzero perpendicular magnetic field the Zeeman effect will break the degeneracy and fix the quantization axis to the z axis.
- The particle-hole (p-h) symmetry. In the spirit of the continuum model we can write a generic wave function of valley η as

$$\Psi_\eta(\mathbf{r}_i) = e^{i\eta n_\theta \mathbf{G}_2 \cdot \mathbf{r}_i} \Psi_{\eta\sigma l}(\mathbf{r}_i) \quad (10)$$

where $e^{i\eta n_\theta \mathbf{G}_2 \cdot \mathbf{r}_i}$ is the rapidly oscillating valley phase ($n_\theta \mathbf{G}_2 \approx \mathbf{K}$, the K point of graphene), and $\Psi_{\eta\sigma l}(\mathbf{r}_i)$ is a smooth envelope that depends on the sublattice σ and layer l of the point \mathbf{r}_i , evaluated at that point. The particle-hole operator $C_{2z}P$ (actually, in the language of Refs. [50, 65], the combined operator of C_{2z} and the particle-hole operator P) is a hermitian operator that squares to the identity and interchanges the graphene valleys, the sublattice and the layer, and is trivial on the spin. It acts on the wave functions as

$$C_{2z}P(\Psi_\eta)(\mathbf{r}_i) = \eta s_l e^{-i\eta n_\theta \mathbf{G}_2 \cdot \mathbf{r}_i} e^{-i\eta \mathbf{G}_2 \cdot \mathbf{r}_i} \Psi_{\eta\bar{\sigma}\bar{l}}(\mathbf{r}_i), \quad (11)$$

where $\bar{\sigma}$ and \bar{l} denote the opposite sublattice and layer to those of \mathbf{r}_i and $s_l = +1$ if l is the top layer and -1 if l is the bottom layer. In the continuum theory, $C_{2z}P$ commutes with the Coulomb interaction and anticommutes with the kinetic energy, hence the name particle-hole operator. As such, it is the generator of a $U(1)$ subgroup in the flat limit, i.e. when the kinetic energy is negligible compared to the Coulomb energy and set to zero.

The $U(1)$ subgroup generated by C_zP and $SU(2)_K \times SU(2)_{K'} \times U(1)_v \times U(1)_c \simeq U(2)_K \times U(2)_{K'}$ do not commute. They are subgroups of the ubiquitous $U(4)$ symmetry of TBG. This $U(4)$ group can be further enlarged to $U(4) \times U(4)$ if we include another $U(1)$ generated by

- the sublattice operator,

$$C = \sum_{i \in A, s} c_{i,s}^\dagger c_{i,s} - \sum_{i \in B, s} c_{i,s}^\dagger c_{i,s}. \quad (12)$$

This operator generates a symmetry in the so-called 'chiral' limit[66], where the projected C operator

in the flat band manifold has eigenvalues ± 1 , i.e. there exists a perfectly sublattice polarized basis of the flat bands. In the real system the polarization is around 0.6-0.8[56], and the symmetry is moderately broken. On the other hand, at one magnetic flux quantum the chiral limit is topologically distinct from the real system[50].

The reader might have noticed that both the valley charge and the $C_{2z}P$ operators are emergent in the continuum theory and do not have a direct analogue in the lattice. In Appendix B we describe our implementation of the valley charge and $C_{2z}P$ in the lattice model.

The irrep basis

The natural basis of the flat bands in the strong coupling analysis is the so-called 'irrep' basis, with the defining property

$$\langle \mathbf{k}\eta\lambda | C_{2z}P | \mathbf{k}\eta'\lambda' \rangle = [\tau_y]_{\eta\eta'} [\lambda_z]_{\lambda\lambda'}, \quad (13)$$

where $\lambda = \pm 1$ is the irrep number. We write $\tau_{0,x,y,z}$ and $\lambda_{0,x,y,z}$ for the identity and Pauli matrices in valley and irrep number space, respectively. In this subsection the spin index is omitted, and we construct two identical copies of the irrep basis, one for each spin polarization.

Given the property $\{C, C_{2z}P\} = 0$, the irrep basis is equivalent to the sublattice polarized basis that diagonalizes the projection of C onto the flat bands, which we denote by $\overline{C}(\mathbf{k})$ for a given momentum \mathbf{k} . The sublattice is labeled by $\sigma = A(+1), B(-1)$, and the identity and Pauli matrices in sublattice space by $\sigma_{0,x,y,z}$. $A(B)$ sublattice has eigenvalue $+1(-1)$ under σ_z .

However, in the real system the particle-hole symmetry is broken, meaning that $\overline{C_{2z}P}(\mathbf{k})$ is not unitary, as we will see. We have to define the irrep basis in a different way.

At zero magnetic field, the sublattice basis is adiabatically connected to the irrep basis of the p-h symmetric limit. This is, if we compute the 'closest' unitary matrix to $\overline{C_{2z}P}(\mathbf{k})$ in the sublattice polarized basis, $[\overline{C_{2z}P}(\mathbf{k})]_{\eta\sigma\eta'\sigma'} = \langle \mathbf{k}\eta\sigma | C_{2z}P | \mathbf{k}\eta'\sigma' \rangle$, we get to a very good accuracy (up to a gauge choice)

$$\overline{C_{2z}P}(\mathbf{k}) \left(\overline{C_{2z}P}(\mathbf{k}) \overline{C_{2z}P}(\mathbf{k})^\dagger \right)^{-1/2} = \sigma_y \tau_x. \quad (14)$$

Hence, if we identify $\lambda = \eta\sigma$ we conclude that indeed both basis are equivalent also with p-h breaking, and they can be used indistinctly. The sublattice polarized bands $|\mathbf{k}\eta\sigma\rangle$ have Chern numbers equal to $\eta\sigma$ [67].

We impose the following $C_{2z}\mathcal{T}$ gauge fixing,

$$\langle \mathbf{k}\rho | C_{2z}\mathcal{T} | \mathbf{k}\rho' \rangle = [\sigma_x \tau_0]_{\rho\rho'}, \quad (15)$$

with ρ the multi-index for valley and sublattice. We also

constrain the representation of C_{2z} and \mathcal{T} ,

$$\begin{aligned} \langle [-\mathbf{k}]\rho | C_{2z} | \mathbf{k}\rho' \rangle &= [\sigma_x \tau_x]_{\rho\rho'} \text{ if } \mathbf{k} \neq [-\mathbf{k}] \text{ or } \mathbf{k} = \mathbf{\Gamma} \\ &= -[\sigma_x \tau_x]_{\rho\rho'} \text{ otherwise,} \\ \langle [-\mathbf{k}]\rho | \mathcal{T} | \mathbf{k}\rho' \rangle &= [\sigma_0 \tau_x]_{\rho\rho'} \text{ if } \mathbf{k} \neq [-\mathbf{k}] \text{ or } \mathbf{k} = \mathbf{\Gamma} \\ &= -[\sigma_0 \tau_x]_{\rho\rho'} \text{ otherwise,} \end{aligned} \quad (16)$$

$[\mathbf{k}]$ being the momentum equivalent to \mathbf{k} inside the Brillouin zone. The additional signs at parity invariant momenta are due to a topological obstruction[33].

Notice that the wave functions are not completely defined, and there exists a phase ambiguity redefining the states as

$$\begin{aligned} |\mathbf{k}\rho\rangle &\longrightarrow [e^{i\alpha(\mathbf{k})\sigma_z\tau_z}]_{\rho\rho'} |\mathbf{k}\rho'\rangle, \\ \alpha(\mathbf{k}) &= \alpha(-\mathbf{k}). \end{aligned} \quad (17)$$

At one magnetic flux quantum the irrep basis is defined by

$$\overline{C_{2z}P}(\mathbf{k}) \left(\overline{C_{2z}P}(\mathbf{k}) \overline{C_{2z}P}(\mathbf{k})^\dagger \right)^{-1/2} = \tau_x \lambda_0. \quad (18)$$

In the continuum model, the chiral limit is topologically distinct from the real system at one flux quantum[50], a phenomenon that is reflected in the tight-binding model. In this case, the irrep basis is not maximally polarized, hence the sublattice polarization and irrep character cannot be simultaneously manifested.

We further fix the representation of C_{2z} to

$$\langle [-\mathbf{k}]\rho | C_{2z} | \mathbf{k}\rho' \rangle = -[\tau_y \lambda_y]_{\rho\rho'}, \quad (19)$$

with ρ now the multi-index for valley and irrep.

Because $C_{2z}\mathcal{T}$ is broken due to the magnetic field, there does not exist a remaining local symmetry to further constrain the basis. As a consequence, in flux the irrep basis is only defined up to arbitrary transformations $V(\mathbf{k})$ in both valleys

$$\begin{aligned} |\mathbf{k}\eta\lambda\rangle &\longrightarrow [V(\mathbf{k})]_{\lambda\lambda'} |\mathbf{k}\eta\lambda'\rangle, \\ V^\dagger([-\mathbf{k}]) \lambda_y V(\mathbf{k}) &= \lambda_y. \end{aligned} \quad (20)$$

IV. EXPLICIT BREAKING OF $U(4)$

The $U(4)$ (or $U(4) \times U(4)$) symmetry is only approximate, and is broken in the atomistic model down to the physical $SU(2)$ of spin rotations. In this section we study the strength of such symmetry breaking.

$SU(2)_K \times SU(2)_{K'}$ and p-h breaking

Assuming that deviations from $[V, C_{2z}P] = 0$ are negligible also in the lattice model, the projected flat limit enjoys the symmetry generated by the p-h operator if the projected $C_{2z}P$ matrix is unitary. Hence, p-h breaking can be quantified by the singular values (s.v.) of

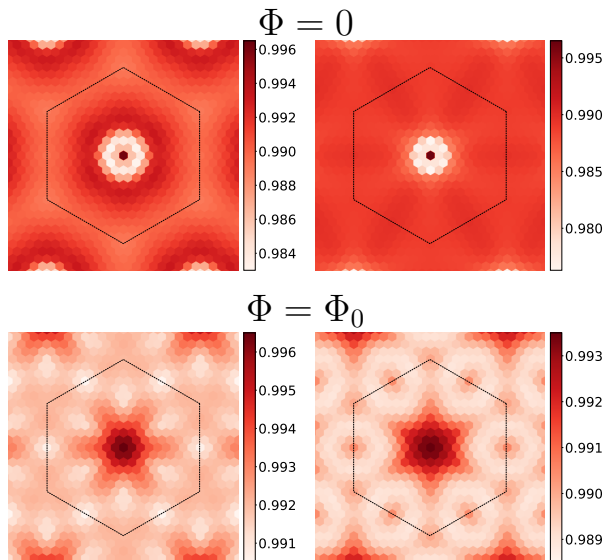


FIG. 5: Singular values of $\overline{C_{2z}P}$ at $\Phi = 0$ and Φ_0 .

They are close to 1, signalling a small particle-hole breaking in the flat bands. For $\Phi = 0$ they were previously computed in Ref. [56]

$\overline{C_{2z}P}(\mathbf{k})$. Deviations from 1 of the s.v. measure the particle-hole asymmetry of the Hilbert space.

The properties $\overline{C_{2z}P}(\mathbf{k})^\dagger = \overline{C_{2z}P}(\mathbf{k})$ and $\{\tau_z, C_{2z}P\} = 0$ force the s.v. to be degenerate in pairs. We plot the largest and smallest s.v. in Fig. 5 at zero and one flux quantum. The deviations are small and similar in both cases, with mean values of around 0.99 and a minimal value of about 0.98 at zero field.

Regarding $U(1)_v$ and $SU(2)_K \times SU(2)_{K'}$, consider the matrix elements of the Coulomb interaction depicted in Fig. 6,

$$V_{abcd} = \langle ab|V|cd\rangle, \quad (21)$$

where the states $|i\rangle$ have valley charge η_i and spin s_i , $i = a, b, c, d$. In the continuum theory, the matrix element is to a first approximation equal to the Fourier transform of $V(\mathbf{r})$ at momentum $\mathbf{q} \sim (\eta_a - \eta_c)\mathbf{K} \sim (\eta_d - \eta_b)\mathbf{K}$, with \mathbf{K} the corner of the graphene BZ, the midpoint of \mathbf{K}_1 and \mathbf{K}_2 in Fig. 2. In turn, V_{abcd} is nonzero only if

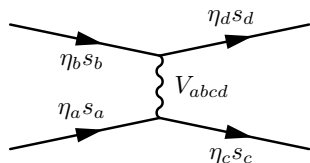


FIG. 6: **Coulomb scattering** between electrons with valley charges $\eta_{a,b,c,d}$ and spin projections $s_{a,b,c,d}$. In the continuum approximation $V_{abcd} \sim V(\mathbf{q})$, with $\mathbf{q} \sim (\eta_a - \eta_c)\mathbf{K} \sim (\eta_d - \eta_b)\mathbf{K}$. Lattice-scale effects distort this approximation.

$\eta_a = \eta_c$ and $\eta_b = \eta_d$ given that $\|\mathbf{K}\| \sim a^{-1} \gg \xi^{-1}$, where ξ is the gate distance in Eq. 5. The valley charge is conserved, $\eta_a + \eta_b = \eta_c + \eta_d$, so $U(1)_v$ is a symmetry. Moreover, the structure of the matrix elements $V_{abcd} \propto \delta_{\eta_a \eta_c} \delta_{\eta_b \eta_d} \delta_{s_a s_c} \delta_{s_b s_d}$ exhibits the symmetry $SU(2)_K \times SU(2)_{K'}$ consisting of independent spin rotations for each valley sector.

For the atomistic model, we show in Appendix C that $U(1)_v$ is preserved but $SU(2)_K \times SU(2)_{K'}$ is broken. Furthermore, it is shown that the exchange energy $-\langle ab|V|ba\rangle$ when $\eta_a = -\eta_b$ is always positive, contributing to an antiferromagnetic Hund's coupling $J < 0$ in the language of Ref. [21].

Moreover, the on-site Hubbard Hamiltonian $U \sum_i n_{i\uparrow} n_{i\downarrow}$ also incorporates symmetry breaking, favouring magnetically ordered phases.

In what follows we quantify the symmetry breaking in the manifold of ground state candidates and discuss its importance.

The manifold of possible ground states

For even values of ν , $\nu = 0, \pm 2$, the ground states in strong coupling are 'U(4) ferromagnets'. Any $U(4)$ rotation U of the valley-spin polarized states is a possible ground state[20, 21, 34, 37, 51]

$$|\text{GS}\rangle = U \left(\prod_{\mathbf{k}} \prod_{j=1, \nu/2+2} d_{\mathbf{k}\eta_j+1s_j}^\dagger d_{\mathbf{k}\eta_j-1s_j}^\dagger |0\rangle \right), \quad (22)$$

$d_{\mathbf{k}\eta\lambda s}^\dagger$ denoting the creation operator of state $|\mathbf{k}\eta\lambda s\rangle$, $|0\rangle$ the state with the filled remote bands, and $s = \uparrow, \downarrow$ the spin index. The identity and Pauli matrices in spin will be denoted by $s_{0,x,y,z}$. The valley-spin flavors η_j, s_j can be chosen arbitrarily, as different choices are related by a $U(4)$ transformation.

The valley polarized states $|\text{VP}\rangle$ correspond to choosing $U = 1$ and $(\eta_1, s_1) = (K, \uparrow)$, $(\eta_2, s_2) = (K, \downarrow)$, $(\eta_3, s_3) = (K', \uparrow)$ above, such that the total valley charge is maximized.

For $\Phi = 0$, the Kramers intervalley coherent (KIVC) state belongs to the $U(4)$ manifold, and is related to the valley polarized (VP) state by a $C_{2z}P$ angle of $\pi/4$

$$|\text{KIVC}\rangle = \exp\left(i\frac{\pi}{4}\mathcal{S}\right)|\text{VP}\rangle, \quad (23)$$

with \mathcal{S} the generator of the particle-hole $U(1)$ in the projected system,

$$\mathcal{S} = \sum_{\mathbf{k}} \sum_{\rho\rho'} c_{\mathbf{k}\rho}^\dagger [\tau_y \lambda_z s_0]_{\rho\rho'} c_{\mathbf{k}\rho'}, \quad (24)$$

again with the multi-index ρ denoting valley, irrep and spin. The unitary $\exp(i\phi\mathcal{S})$ transforms the basis as

$$e^{i\phi\mathcal{S}} d_{\mathbf{k}\rho}^\dagger e^{-i\phi\mathcal{S}} = \left[\exp\left(i\phi(\tau_y \lambda_z s_0)^T\right) \right]_{\rho\rho'} d_{\mathbf{k}\rho'}^\dagger. \quad (25)$$

On another hand, the chiral $U(4) \times U(4)$ group contains operations that rotate each Chern sector independently[41]. The time reversal intervalley coherent (TIVC) order relates to VP via a $U(4) \times U(4)$ rotation with $C_{2z}P$ angles of $+\pi/4$ and $-\pi/4$,

$$|\text{TIVC}\rangle = \exp\left(i\frac{\pi}{4}\mathcal{S}_{+1} - i\frac{\pi}{4}\mathcal{S}_{-1}\right)|\text{VP}\rangle. \quad (26)$$

Here $\mathcal{S}_\lambda = P_\lambda \mathcal{S} P_\lambda$, with P_λ the projector onto irrep λ .

In addition, particularizing to $\nu = 0$ we consider the fully spin polarized (SP) state,

$$|\text{SP}\rangle = \prod_{\mathbf{k}} d_{\mathbf{k}K+1\uparrow}^\dagger d_{\mathbf{k}K-1\uparrow}^\dagger d_{\mathbf{k}K'+1\uparrow}^\dagger d_{\mathbf{k}K'-1\uparrow}^\dagger |0\rangle, \quad (27)$$

that is derived from the valley-spin polarized (VSP) state,

$$|\text{VSP}\rangle = \prod_{\mathbf{k}} d_{\mathbf{k}K+1\uparrow}^\dagger d_{\mathbf{k}K-1\uparrow}^\dagger d_{\mathbf{k}K'+1\downarrow}^\dagger d_{\mathbf{k}K'-1\downarrow}^\dagger |0\rangle, \quad (28)$$

after a spin rotation in valley K' , belonging to $SU(2)_{K'} \times SU(2)_{K'}$.

$$|\text{SP}\rangle = \exp\left(i\frac{\pi}{2}P_{K'}s_yP_{K'}\right)|\text{VSP}\rangle, \quad (29)$$

with $P_{K'}$ the projector onto valley K' . At zero field, by \mathcal{T} symmetry the VP and the VSP states have the same energy.

At $\Phi = \Phi_0$, the intervalley coherent state corresponds to a $C_{2z}P$ rotation of the VP, of angle $\pi/4$,

$$|\text{IVC}\rangle = \exp\left(i\frac{\pi}{4}\mathcal{S}\right)|\text{VP}\rangle, \quad (30)$$

with \mathcal{S} taking a different form in accordance with our gauge choice of Eq. 18,

$$\mathcal{S} = \sum_{\mathbf{k}} \sum_{\rho\rho'} c_{\mathbf{k}\rho}^\dagger [\lambda_0 \tau_x s_0]_{\rho\rho'} c_{\mathbf{k}\rho'}. \quad (31)$$

Explicit symmetry breaking in the ground state manifold

The strength of the explicit symmetry breaking processes can be measured by the difference in Coulomb energy of the different ground state candidates. In Tables F2 and F1 of Appendix F we tabulate the different contributions to the total energy (Hartree, Fock, kinetic and Hubbard energy) of the states discussed above. We note that, remarkably, the kinetic energy is degenerate for all the states considered at a given filling. Here we focus on the states at charge neutrality.

At $\Phi = 0$, p-h breaking corresponds to the difference between VP and KIVC energies,

$$\epsilon(\langle V \rangle_{\text{VP}} - \langle V \rangle_{\text{KIVC}})/N_M = 2.26 \text{ meV}, \quad (32)$$

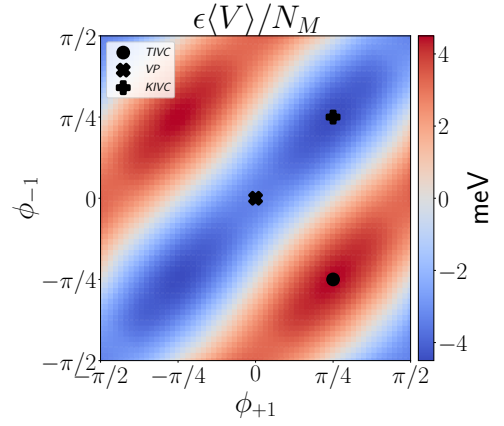


FIG. 7: Breaking of the chiral $U(4) \times U(4)$ symmetry. Coulomb energy (ϵ is set to 1) per unit cell of candidates states in the $U(4) \times U(4)$ manifold at filling $\nu = -2$, which is explicitly broken to $U(4)$ with $\phi_{+1} = \phi_{-1}$. The zero point of the energy is arbitrary. VP, KIVC and TIVC are the valley polarized, Kramers intervalley coherent and time reversal intervalley coherent states, respectively. Sending $\phi_{\pm 1} \rightarrow -\phi_{\pm 1}$ amounts to a $U(1)_v$ transformation of angle π . $U(1)_v$ is visibly preserved.

the breaking of the chiral symmetry by the difference between VP and TIVC states,

$$\epsilon(\langle V \rangle_{\text{TIVC}} - \langle V \rangle_{\text{VP}})/N_M = 14.01 \text{ meV}, \quad (33)$$

and the breaking of $SU(2)_K \times SU(2)_{K'}$ by the energies of VSP (same energy as VP) and SP,

$$\epsilon(\langle V \rangle_{\text{SP}} - \langle V \rangle_{\text{VP}})/N_M = 10.32 \text{ meV}. \quad (34)$$

Here N_M is the number of unit cells, and we have multiplied by ϵ so that we are comparing energies per unit cell for $\epsilon = 1$.

Very similarly for $\Phi = \Phi_0$, p-h breaking corresponds to the difference between VP and IVC energies,

$$\epsilon(\langle V \rangle_{\text{IVC}} - \langle V \rangle_{\text{VP}})/N_M = 0.74 \text{ meV}, \quad (35)$$

and the breaking of $SU(2)_K \times SU(2)_{K'}$ by the VSP and SP states,

$$\epsilon(\langle V \rangle_{\text{SP}} - \langle V \rangle_{\text{VSP}})/N_M = 5.23 \text{ meV}. \quad (36)$$

Additionally, in Fig. 7 we plot the Coulomb energy of states of the form $\exp(i\phi_{+1}\mathcal{S}_{+1} + i\phi_{-1}\mathcal{S}_{-1})|\text{VP}\rangle$ for $\nu = -2$ and $B = 0$ T. The breaking of the chiral $U(4) \times U(4)$ symmetry down to $U(4)$ is evident, and the inversion symmetry of the plot shows the conservation of $U(1)_v$.

In light of the results, we conclude that $C_{2z}P$ breaking is smaller than the breaking of the chiral symmetry at $\Phi = 0$ and of $SU(2)_K \times SU(2)_{K'}$.

The $SU(2)_K \times SU(2)_{K'}$ breaking is stronger and comparable to the breaking of the chiral symmetry at zero

field. This effect was called intervalley Hund's interaction in Ref. [21], where it was argued that it is the smallest energy scale in the hierarchy of symmetry breakings. Our calculations in the tight-binding model involve lattice-scale interactions, providing reliable values for the splitting of the $SU(2)_K \times SU(2)_{K'}$ multiplets[68].

The Hubbard interaction clearly breaks $SU(2)_K \times SU(2)_{K'}$, and favours the states with a net spin polarization. On the other hand, we showed that the long ranged Coulomb energy is Hund antiferromagnetic, supporting states with opposite spins in different valleys. Although in the real system we expect their values to be correlated, the interplay between U and ϵ (and possibly other effects due to phonons[68]) determines the sign of the Hund's coupling J . For instance, the splitting between the VSP and SP states changes sign when $\epsilon U = 8.82$ eV(9.02 eV) at zero field(one flux quantum). Also, if the Hubbard interaction is strong enough, it can go beyond selecting the state of the $SU(2)_K \times SU(2)_{K'}$ multiplets and stabilize spin polarized phases, as we will see.

Finally, notice that the small $C_{2z}P$ breaking favours the KIVC phase as can be seen in Fig. 7 or Eq. 32. However, the gain in energy of the 'dressed' self-consistent states is larger than this small splitting between the VP and KIVC, so the p-h breaking is not the decisive factor in the stability of the ground states.

V. SELF-CONSISTENT HARTREE-FOCK

We have carried out self-consistent Hartree-Fock simulations in a system of 12×12 unit cells, focusing on filling factors $\nu = -2, 0, +2$. We describe the Hartree-Fock formalism and the flat band projection method in Appendix D.

Typical values for ϵ found in the literature range from about 7 to 12[21, 26], so we choose $\epsilon = 10$ and a realistic value for U of 4 eV[27, 42]. However, it has been argued that internal screening is large in these systems and a more appropriate value for ϵ is several times larger[27, 69]. This agrees with the fact that lower values of ϵ overestimate the gap of the insulators, which in transport are found to be $\lesssim 1$ meV[3–5, 38, 52]. We account for both scenarios and report results also for $\epsilon = 50$ and 0.5 eV.

The self-consistent states are characterized by the Q matrix, defined by

$$\begin{aligned} [Q(\mathbf{k})]_{\rho\rho'} &= 2[P(\mathbf{k})]_{\rho\rho'} - \delta_{\rho\rho'}, \\ [P(\mathbf{k})]_{\rho\rho'} &= \langle d_{\mathbf{k}\rho}^\dagger d_{\mathbf{k}\rho'} \rangle, \end{aligned} \quad (37)$$

with the properties $Q(\mathbf{k}) = Q(\mathbf{k})^\dagger$, $Q(\mathbf{k})^2 = 1$ and $\text{tr}(Q(\mathbf{k})) = 2\nu$. In most cases, as we discuss below, Q will be diagonal in the spin, $Q(\mathbf{k}) = Q_\uparrow(\mathbf{k})P_\uparrow + Q_\downarrow(\mathbf{k})P_\downarrow$ ($P_{\uparrow(\downarrow)}$ is the projector onto spin $\uparrow(\downarrow)$), with each spin polarization either completely empty ($Q_s(\mathbf{k}) = -1$), completely full ($Q_s(\mathbf{k}) = +1$) or half filled. If half filled, Q_s can be expressed as a linear combination of products of

Pauli matrices,

$$Q_s(\mathbf{k}) = \sum_{\substack{\alpha,\beta=0,x,y,z \\ (\alpha,\beta) \neq (0,0)}} A_{\alpha\beta}^s(\mathbf{k}) \sigma_\alpha \tau_\beta = \sum_{\substack{\alpha,\beta=0,x,y,z \\ (\alpha,\beta) \neq (0,0)}} B_{\alpha\beta}^s(\mathbf{k}) \lambda_\alpha \tau_\beta, \quad (38)$$

with $A_{\alpha\beta}^s(\mathbf{k})$, $B_{\alpha\beta}^s(\mathbf{k})$ real coefficients and $\sum_{\alpha\beta} (A_{\alpha\beta}^s(\mathbf{k}))^2 = \sum_{\alpha\beta} (B_{\alpha\beta}^s(\mathbf{k}))^2 = 1$. In the following we will write $\langle \sigma_\alpha \tau_\beta \rangle$, $\langle \lambda_\alpha \tau_\beta \rangle$ to denote the coefficients $A_{\alpha\beta}^s(\mathbf{k})$, $B_{\alpha\beta}^s(\mathbf{k})$. The momentum dependence is left implicit, and the spin can be deduced depending on the context.

The preferred state of the analytical approaches and numerical studies at zero magnetic field is the KIVC[21, 22, 34, 36]. At $\nu = 0$ it can be either spin singlet, $Q(\mathbf{k}) = \sigma_y \tau_y$, or 'spin triplet', $Q(\mathbf{k}) = \sigma_y \tau_y \mathbf{n} \cdot \mathbf{s}$, with \mathbf{n} denoting an spontaneous direction. An antiferromagnetic Hund's coupling, $J < 0$, favours the KIVC singlet whereas $J > 0$ prefers the 'triplet'[21]. However, in our Hartree Fock numerics we restrict the state to be a direct product of spin up and spin down wave functions, so Q will be diagonal in the spin index and we cannot access the 'triplet' state. Setting $\mathbf{n} = \hat{z}$ amounts to a valley rotation which does not change the kinetic or Coulomb energy. By a similar argument to the one given in Appendix D, the Hubbard energy does not change either.

For $\nu = \pm 2$, a ferromagnetic Hund's coupling leads to $Q(\mathbf{k}) = \sigma_y \tau_y P_\uparrow \pm P_\downarrow$ where the spins in both valleys are aligned. Antiferromagnetic coupling on the other hand promotes the state where the spins of the two valleys are anti-aligned. Again, we can only detect the spin-diagonal order.

Notice that the $U(1)_v$ symmetry allows for an arbitrary global rotation in the order parameter, $\tau_y \rightarrow \cos(\theta)\tau_y + \sin(\theta)\tau_x$. However, the difference in the intervalley angle for different values of \mathbf{k} cannot be removed

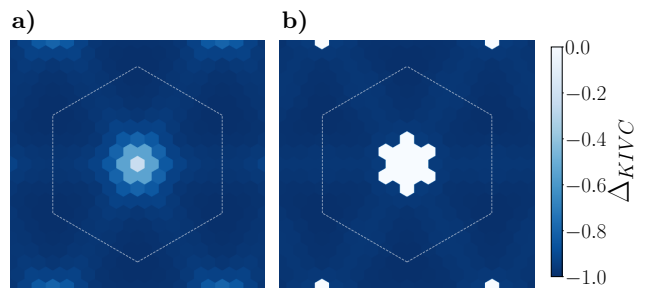


FIG. 8: KIVC order at $\Phi = 0$. **a)** Δ_{KIVC} at $\nu = +2$ and $\epsilon = 10, U = 4$ eV. The inter-Chern parameter completes the total weight, $\Delta_{\text{IC}} = 1 - (\Delta_{\text{KIVC}})^2$, reaching a value of 0.95 at Γ_M . In the case of $\epsilon = 50, U = 0.5$ eV the only difference is that Δ_{IC} is smaller with a maximal value of 0.46 at Γ_M . For $\nu = 0$ the order parameter is almost identical. **b)** KIVC order parameter at $\nu = -2$ and $\epsilon = 50, U = 0.5$ eV. Around Γ_M there are extra holes creating a Fermi pocket, and the order parameter is ill-defined in that region.

and is physical. In any case, we do not observe textures or windings in the IVC angle.

Contrary to the the BM theory[42], in the tight-binding model the on-site Hubbard interaction is implemented naturally. At charge neutrality the SP state is not competitive if we consider only the Coulomb energy, but for sufficiently large U it will be the lowest energy state. For electron and hole dopings, the candidate states are spin polarized, see Table F2 in Appendix F, and the pre-

ferred states (KIVC, VP) are degenerate in H_U , so we do not expect different orders for different U .

At flux Φ_0 , analytical studies[51] suggest that the Zeeman energy drives the system to maximize the spin polarization in the $U(4)$ manifold. At charge neutrality the SP state with $Q(\mathbf{k}) = s_z$ is the ground state and at $\nu = -2(+2)$ there are two possible orders, IVC, with $Q(\mathbf{k}) = \lambda_0 \tau_y P_\uparrow - P_\downarrow (\lambda_0 \tau_y P_\downarrow + P_\uparrow)$, or valley polarization, $Q(\mathbf{k}) = \lambda_0 \tau_z P_\uparrow - P_\downarrow (\lambda_0 \tau_z P_\downarrow + P_\uparrow)$.

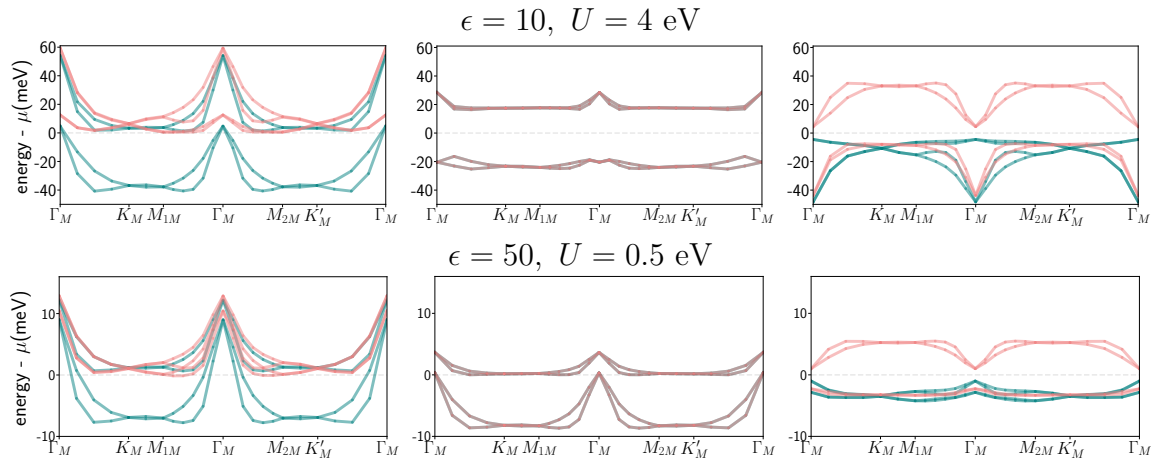


FIG. 9: **KIVC band structures of MATBG at $B = 0$ T.** Different spins are shown in different colors. From left to right, the filling is $\nu = -2, 0, +2$. At $\nu = \pm 2$ these are the true ground states, whereas at charge neutrality there is competition between the KIVC and the spin polarized state. The many-body electron-hole asymmetry is apparent.

Results for $\Phi = 0$

Examining Table F2 we deduce that the possible orders for $B = 0$ T are the VP or KIVC, or the SP at charge neutrality. We compute self-consistent states with initial guesses for the KIVC, VP and SP orders, whose energies are tabulated in Table F4 of Appendix F. We plot the band structures of the KIVC states in Fig. 9, of the SP states in Fig. 10 and of the VP states in Fig. E.6 of Appendix E. The KIVC, with order parameter

$$\Delta_{\text{KIVC}} = \langle \sigma_y \tau_y \rangle, \quad (39)$$

is the ground state for $\nu = \pm 2$, and the KIVC and SP are competitive at charge neutrality.

A general feature of the self-consistent states is that deviations from the predominant order parameter occur near the Γ_M point.

In the gapped phases they involve the inter-Chern parameter,

$$\Delta_{\text{IC}} = \langle \sigma_x \tau_0 \rangle^2 + \langle \sigma_y \tau_z \rangle^2, \quad (40)$$

signalling coherent superpositions of bands with different Chern numbers. Notice how the expression for Δ_{IC} is invariant with respect to the gauge ambiguity of Eq. 17. The effect of Δ_{IC} near Γ_M is to reduce the exchange energy at the expense of kinetic (and Hartree for $\nu = \pm 2$) energy. In consequence, Δ_{IC} becomes larger for lower ϵ ,

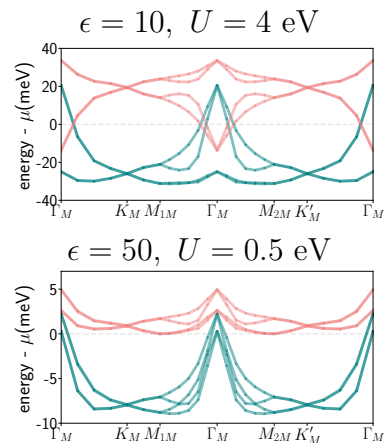


FIG. 10: **Band structures of the spin polarized phase at charge neutrality.** Different spins are shown with different colors. The spin polarization is not full, and the system is a metal.

where the kinetic energy penalty is comparatively less important.

For $\nu = -2$ the system is metallic with a hole pocket around Γ_M . Because the states near Γ_M show a homogeneous density profile, the Hartree energy is optimized if the excess density relative to charge neutrality originates from this region of the Brillouin zone. This is manifested

by the characteristic dips at electron doping, or rises at hole doping in the band structures[70]. At $\nu = -2$ the holes are populated, optimizing the Hartree energy.

In Fig. 8 we plot the KIVC order parameter for two different cases, where both phenomena are illustrated. Additionally, as depicted in Fig. 10 the bands of the spin polarized states show also the Fermi pockets at Γ_M , and the additional electrons and holes appear in inter-Chern coherence.

The different behaviour at $\nu = +2$ and $\nu = -2$ is a sign of the many-body electron-hole asymmetry, which is a robust experimental feature[3, 4, 38]. We argue that the flat band limit shows electron-hole symmetry but the kinetic energy disturbs it at weaker couplings. Indeed, the H_0 spectrum is very asymmetric at zero flux, see Fig. 3. At Φ_0 flux the spectrum is visibly more p-h symmetric, and the electron-hole relation between $\nu = +2$ and -2 is more apparent for $\epsilon = 10, U = 4$ eV (Fig. 13).

Let us now discuss the energies of the different self-consistent phases at charge neutrality. In the tables below we write the energies of the KIVC, SP and VP self-consistent states at relative to the pure KIVC state, in meV per unit cell (the value of U is in units of eV).

$\epsilon = 10, U = 4$ eV					
	$\epsilon \times \text{Hartree}$	$\epsilon \times \text{Fock}$	Hubb./ U	kinetic	total
KIVC	-0.49	-64.60	0.01	1.28	-5.19
SP	-0.13	-8.19	-1.10	0.61	-4.62
VP	-0.13	-17.97	0.00	0.61	-1.20

$\epsilon = 50, U = 0.5$ eV					
	$\epsilon \times \text{Hartree}$	$\epsilon \times \text{Fock}$	Hubb./ U	kinetic	total
KIVC	-0.91	-31.14	0.00	0.40	-0.24
SP	-0.67	18.61	-1.13	-0.16	-0.37
VP	-0.67	8.48	0.00	-0.16	-0.00

The KIVC always has lower energy than the VP state, but the competition between KIVC and SP is more complex. For $\epsilon = 10, U = 4$ eV the KIVC state is 0.57 meV per unit cell lower than the SP state, whereas for $\epsilon = 50, U = 0.5$ eV the SP state is the ground state with 0.13 meV/cell of difference. Assuming that the self-consistent state does not change much with U (as a matter of fact, we find that the states for $\epsilon = 10, U = 4$ are almost identical to those with $\epsilon = 10, U = 0.5$ eV), we expect a transition to the SP state for U greater than a critical value of $U_c = 4.51$ eV when $\epsilon = 10$, and to the KIVC for U smaller than $U_c = 0.39$ when $\epsilon = 50$.

Results for $\Phi = \Phi_0$

The energies of self-consistent states for $\Phi = \Phi_0$ are tabulated in Table F3 of Appendix F, and their band structures plotted in Fig. 13. The spin polarization is maximal for all fillings, however, we observe gapped

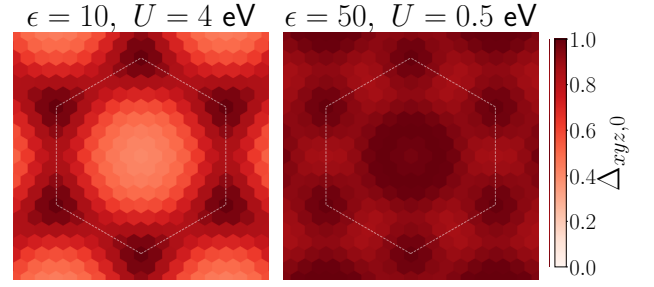


FIG. 11: **The order parameter for $\nu = -2$ at $\Phi = \Phi_0$.** The dominant order parameter of the self-consistent states, $\Delta_{xyz,0}$, is shown. For $\epsilon = 10$ it is very similar to its many-body partner at $\nu = +2$ in Fig. 12. The $\Delta_{xyz,0}$ character is enhanced for weaker couplings.

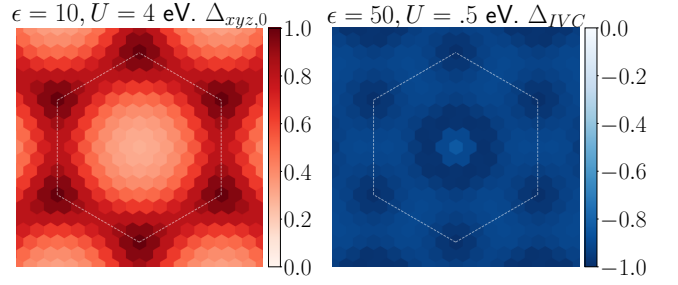


FIG. 12: **Phase transition at $\nu = +2$ and $\Phi = \Phi_0$.** The order parameters of the self-consistent states are shown for $\epsilon = 10, U = 4$ eV and $\epsilon = 50, U = 0.5$ eV. For some value of ϵ between 50 and 30 there is a transition from the IVC to the $\Delta_{xyz,0}$ state.

phases with a completely different order compared to the previously predicted for $\nu = \pm 2$.

The order parameter

$$\Delta_{xyz,0} = \langle \lambda_x \tau_0 \rangle^2 + \langle \lambda_y \tau_0 \rangle^2 + \langle \lambda_z \tau_0 \rangle^2, \quad (41)$$

which is invariant under the gauge ambiguity of Eq. 20, is predominant at hole doping. $\Delta_{xyz,0}$ corresponds to choosing a particular irrep basis allowed by Eq. 20, and filling the bands with the same irrep number of the two valleys.

At electron doping, the state for $\epsilon = 10, U = 4$ eV is very similar to the many-body particle-hole partner of the $\nu = -2$ insulator, with the same order parameter. On the other hand, when ϵ is larger than some critical value between 30 and 50, see Appendix E, there is a phase transition that promotes the IVC state. For both $\epsilon = 10, U = 4$ eV and $\epsilon = 50, U = 0.5$ eV the second largest order parameter is found to be $\Delta_{xyz,z}$, which is obtained after replacing τ_0 by τ_z in Eq. 41. The total 'spectral weight' is essentially saturated by the two terms.

Let us discuss the discrepancies between our numerical results and the results of Ref. [51]. Firstly, the kinetic spectrum at $B = 26.5$ T is much broader than at zero field, with a gap between the valence and conduction

bands of about 4 meV. The system is in an intermediate coupling regime as the kinetic energy is comparable to the interaction energy. Secondly, at $B = 0$ T the order is exchange-driven (at least at fillings $\nu = \pm 2$ when the Hubbard term is not relevant), and the Fock energy is optimized in the ground state. For $B = 26.5$ T we find that the direct term is more influential. In Ref. [51] the ‘flat metric condition’ assumes that the Hartree energy is trivial, and the strong coupling analysis suggests that the kinetic energy is a subdominant scale. Both premises are at odds with our numerical results in the tight-binding model.

The ground state at hole doping has Chern number -2 and is adiabatically connected to the ground state of the non interacting Hamiltonian. The predominant order parameter, $\Delta_{xyz,0}$, is plotted in Fig. 11. In the following table we write the energy gain of the $\nu = -2$ ground states with respect to the candidate IVC state for $\epsilon = 10$, $U = 4$ eV and $\epsilon = 50$, $U = 0.5$ eV, in meV per unit cell (U is expressed in eV).

$\nu = -2$						
ϵ, U	$\epsilon \times \text{Hartree}$	$\epsilon \times \text{Fock}$	Hubb./ U	kinetic	total	
10, 4	-100.27	-41.38	-0.13	-2.89	-17.58	
50, 0.5	-105.80	19.14	-0.15	-4.94	-6.75	

Clearly, the Hartree and kinetic energies drive the system towards a different order to the previously proposed.

On the other hand, we write in the table below the energy differences of the self-consistent states for $\nu = +2$ and the pure IVC state.

$\nu = +2$						
ϵ, U	$\epsilon \times \text{Hartree}$	$\epsilon \times \text{Fock}$	Hubb./ U	kinetic	total	
10, 4	-155.20	-3.40	-0.26	5.21	-11.69	
50, 0.5	-1.65	-9.29	0.00	-0.19	-0.41	

In this case, we conclude that the interplay between the Hartree and kinetic energies determines the transition between the two competing orders, with their order parameters plotted in Fig. 12. The phase transition at intermediate values of ϵ is topological, since the state for $\epsilon = 10$, $U = 4$ eV is found to have Chern number +2, and the IVC state is trivial with Chern number 0.

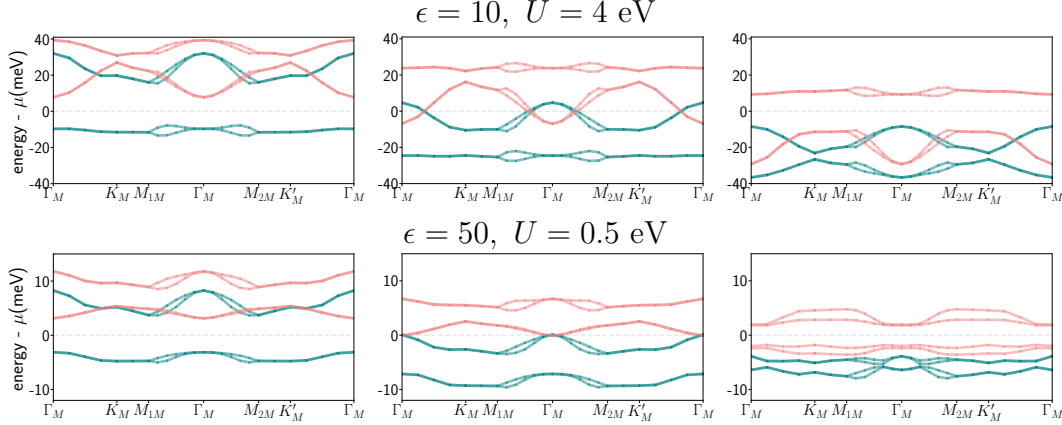


FIG. 13: **Quasiparticle band structures of MATBG at $B = 26.5$ T.** Spin up bands are shown in blue and spin down bands in red. From left to right, the filling factor is $\nu = -2, 0, +2$. The states are metallic at charge neutrality and insulating for electron and hole doping. When $\epsilon = 10, U = 4$ eV the $\nu = \pm 2$ states are related by a particle-hole transformation.

VI. CONCLUSIONS

In this work, we have studied magic angle twisted bilayer graphene under external magnetic fluxes of zero and one flux quantum per unit cell, and dopings of $-2, 0$ and $+2$ electrons per unit cell. In the atomistic tight-binding model we capture details of the physics that are not available in continuum theories.

For instance, we have established numerically and analytically that the long ranged Coulomb interaction contributes to an antiferromagnetic intervalley Hund’s coupling. The on-site Hubbard term, which is generally not included in the continuum model[42], contributes to a

ferromagnetic coupling. The character of these valley exchanging interactions is important for the superconducting order parameter in Moiré systems[71–73].

In addition, we studied the particle-hole asymmetry of the Hilbert space of the flat bands, and concluded that p-h breaking effects represent a small energy scale in the problem. In particular, the effects of p-h breaking cannot stabilize the time reversal intervalley coherent (TIVC) state at $\nu = -2$ observed recently[40], and it must rely on other mechanisms like electron-phonon coupling[36, 74].

In order to elucidate the nature of the ground state we have performed self-consistent Hartree-Fock simulations. For $\Phi = 0$, the Kramers intervalley coherent state is the

ground state at electron and hole doping, and is competitive with the spin polarized state, supported by the Hubbard energy, at charge neutrality. In contrast to the BM model, where the self-consistent KIVC is favoured by kinetic energy superexchange[20–22, 32, 34, 36], in the tight-binding model the inter-Chern order at Γ_M lowers the exchange at the expense of kinetic and Hartree energies. Also, in the BM model the on-site Hubbard interaction is generally not included[42], and the SP state is never a candidate. We predict a phase transition from the KIVC to the SP at a critical value of $U_c = 4.51$ eV when $\epsilon = 10$. Finally, we also detect the many-body electron-hole asymmetry found in the experiments[3, 4, 38].

For Φ_0 flux, the self-consistent states are spin polarized due to the Zeeman effect. Also, the Dirac cones are gapped and the bandwidth of the flat bands is increased, driving the system to an intermediate coupling regime. There are correlated insulators for $\nu = \pm 2$, and at charge neutrality the state is (almost) fully spin polarized. For electron doping and small screening, we observe an insulator with Chern number +2, consistent with experiments[52], and a trivial insulator for large screening. We envision the possibility of observing a topological phase transition by changing the screening environment in the experimental setup.

Strain[36, 39] and electron-phonon coupling[22, 43, 74] are relevant to the physics and their treatment is left for future work. Also, an accurate understanding of internal screening is needed, and it has been suggested that it is large in MATBG[27, 75]. Improvements of the Hartree-Fock method such as the inclusion of more bands in the projection, and specially allowing for coherence between spins, like in the KIVC 'triplet' state, will further refine the outcome.

Finally, our results shed light into the correlated states in magic angle twisted bilayer graphene with precise atomic-scale modelling, both at $B = 0$ and 26.5 T. Furthermore, our calculations constitute the first self-consistent study of the correlated phases in MATBG under one magnetic flux quantum.

VII. ACKNOWLEDGEMENTS

This work has been supported by MICINN (Spain) under Grant No. PID2020-113164GB-I00, as well as by the CSIC Research Platform on Quantum Technologies PTI-001. The access to computational resources of CESGA (Centro de Supercomputación de Galicia) is also gratefully acknowledged.

-
- [1] M. Polini, F. Giazotto, K. C. Fong, I. M. Pop, C. Schuck, T. Boccali, G. Signorelli, M. D'Elia, R. H. Hadfield, V. Giovannetti, D. Rossini, A. Tredicucci, D. K. Efetov, F. H. L. Koppens, P. Jarillo-Herrero, A. Grassellino, and D. Pisignano, *Materials and devices for fundamental quantum science and quantum technologies* (2022).
- [2] Y. Cao, V. Fatemi, S. Fang, K. Watanabe, T. Taniguchi, E. Kaxiras, and P. Jarillo-Herrero, Unconventional superconductivity in magic-angle graphene superlattices, *Nature* **556**, 43 (2018).
- [3] M. Yankowitz, S. Chen, H. Polshyn, Y. Zhang, K. Watanabe, T. Taniguchi, D. Graf, A. F. Young, and C. R. Dean, Tuning superconductivity in twisted bilayer graphene, *Science* **363**, 1059 (2019), <https://www.science.org/doi/pdf/10.1126/science.aav1910>.
- [4] X. Lu, P. Stepanov, W. Yang, M. Xie, M. A. Aamir, I. Das, C. Urgell, K. Watanabe, T. Taniguchi, G. Zhang, A. Bachtold, A. H. MacDonald, and D. K. Efetov, Superconductors, orbital magnets and correlated states in magic-angle bilayer graphene, *Nature* **574**, 653 (2019).
- [5] X. Liu, Z. Wang, K. Watanabe, T. Taniguchi, O. Vafek, and J. I. A. Li, Tuning electron correlation in magic-angle twisted bilayer graphene using coulomb screening, *Science* **371**, 1261 (2021), <https://www.science.org/doi/pdf/10.1126/science.abb8754>.
- [6] A. Jaoui, I. Das, G. Di Battista, J. Díez-Mérida, X. Lu, K. Watanabe, T. Taniguchi, H. Ishizuka, L. Levitov, and D. K. Efetov, Quantum critical behaviour in magic-angle twisted bilayer graphene, *Nature Physics* **18**, 633 (2022).
- [7] Y. Cao, D. Chowdhury, D. Rodan-Legrain, O. Rubies-Bigorda, K. Watanabe, T. Taniguchi, T. Senthil, and P. Jarillo-Herrero, Strange metal in magic-angle graphene with near planckian dissipation, *Phys. Rev. Lett.* **124**, 076801 (2020).
- [8] S. Wu, Z. Zhang, K. Watanabe, T. Taniguchi, and E. Y. Andrei, Chern insulators, van hove singularities and topological flat bands in magic-angle twisted bilayer graphene, *Nature Materials* **20**, 488 (2021).
- [9] P. Stepanov, M. Xie, T. Taniguchi, K. Watanabe, X. Lu, A. H. MacDonald, B. A. Bernevig, and D. K. Efetov, Competing zero-field chern insulators in superconducting twisted bilayer graphene, *Phys. Rev. Lett.* **127**, 197701 (2021).
- [10] Y. Xie, A. T. Pierce, J. M. Park, D. E. Parker, E. Khalaf, P. Ledwith, Y. Cao, S. H. Lee, S. Chen, P. R. Forrester, K. Watanabe, T. Taniguchi, A. Vishwanath, P. Jarillo-Herrero, and A. Yacoby, Fractional chern insulators in magic-angle twisted bilayer graphene, *Nature* **600**, 439 (2021).
- [11] C. Repellin and T. Senthil, Chern bands of twisted bilayer graphene: fractional chern insulators and spin phase transition (2019), [arXiv:1912.11469 \[cond-mat.str-el\]](https://arxiv.org/abs/1912.11469).
- [12] P. J. Ledwith, G. Tarnopolsky, E. Khalaf, and A. Vishwanath, Fractional chern insulator states in twisted bilayer graphene: An analytical approach, *Phys. Rev. Res.* **2**, 023237 (2020).
- [13] A. Chew, Y. Wang, B. A. Bernevig, and Z.-D. Song, Higher-order topological superconductivity in twisted bilayer graphene, *Phys. Rev. B* **107**, 094512 (2023).
- [14] L. Wang, E.-M. Shih, A. Ghiotto, L. Xian, D. A. Rhodes, C. Tan, M. Claassen, D. M. Kennes, Y. Bai, B. Kim, K. Watanabe, T. Taniguchi, X. Zhu, J. Hone, A. Rubio, A. N. Pasupathy, and C. R. Dean, Correlated elec-

- tronic phases in twisted bilayer transition metal dichalcogenides, *Nature Materials* **19**, 861 (2020).
- [15] J. M. Park, Y. Cao, K. Watanabe, T. Taniguchi, and P. Jarillo-Herrero, Tunable strongly coupled superconductivity in magic-angle twisted trilayer graphene, *Nature* **590**, 249 (2021).
- [16] M. G. Scheer and B. Lian, Twistronics of kekulé graphene: Honeycomb and kagome flat bands (2023), [arXiv:2305.19927](https://arxiv.org/abs/2305.19927) [cond-mat.mes-hall].
- [17] V. Crépel, A. Dumbrack, D. Guerci, J. Bonini, and J. Cano, Chiral model of twisted bilayer graphene realized in a monolayer (2023), [arXiv:2305.14423](https://arxiv.org/abs/2305.14423) [cond-mat.mes-hall].
- [18] Y. Cao, V. Fatemi, A. Demir, S. Fang, S. L. Tomarken, J. Y. Luo, J. D. Sanchez-Yamagishi, K. Watanabe, T. Taniguchi, E. Kaxiras, R. C. Ashoori, and P. Jarillo-Herrero, Correlated insulator behaviour at half-filling in magic-angle graphene superlattices, *Nature* **556**, 80 (2018).
- [19] H. C. Po, L. Zou, A. Vishwanath, and T. Senthil, Origin of mott insulating behavior and superconductivity in twisted bilayer graphene, *Phys. Rev. X* **8**, 031089 (2018).
- [20] J. Kang and O. Vafek, Strong coupling phases of partially filled twisted bilayer graphene narrow bands, *Phys. Rev. Lett.* **122**, 246401 (2019).
- [21] N. Bultinck, E. Khalaf, S. Liu, S. Chatterjee, A. Vishwanath, and M. P. Zaletel, Ground state and hidden symmetry of magic-angle graphene at even integer filling, *Phys. Rev. X* **10**, 031034 (2020).
- [22] Y. H. Kwan, G. Wagner, T. Soejima, M. P. Zaletel, S. H. Simon, S. A. Parameswaran, and N. Bultinck, Kekulé spiral order at all nonzero integer fillings in twisted bilayer graphene, *Phys. Rev. X* **11**, 041063 (2021).
- [23] P. Stepanov, I. Das, X. Lu, A. Fahimniya, K. Watanabe, T. Taniguchi, F. H. L. Koppens, J. Lischner, L. Levitov, and D. K. Efetov, Untying the insulating and superconducting orders in magic-angle graphene, *Nature* **583**, 375 (2020).
- [24] A. L. Sharpe, E. J. Fox, A. W. Barnard, J. Finney, K. Watanabe, T. Taniguchi, M. A. Kastner, and D. Goldhaber-Gordon, Evidence of orbital ferromagnetism in twisted bilayer graphene aligned to hexagonal boron nitride, *Nano Letters* **21**, 4299 (2021), pMID: 33970644, <https://doi.org/10.1021/acs.nanolett.1c00696>.
- [25] A. L. Sharpe, E. J. Fox, A. W. Barnard, J. Finney, K. Watanabe, T. Taniguchi, M. A. Kastner, and D. Goldhaber-Gordon, Emergent ferromagnetism near three-quarters filling in twisted bilayer graphene, *Science* **365**, 605 (2019).
- [26] S. Zhang, X. Lu, and J. Liu, Correlated insulators, density wave states, and their nonlinear optical response in magic-angle twisted bilayer graphene, *Phys. Rev. Lett.* **128**, 247402 (2022).
- [27] J. González and T. Stauber, Magnetic phases from competing hubbard and extended coulomb interactions in twisted bilayer graphene, *Phys. Rev. B* **104**, 115110 (2021).
- [28] J. González and T. Stauber, Time-reversal symmetry breaking versus chiral symmetry breaking in twisted bilayer graphene, *Phys. Rev. B* **102**, 081118 (2020).
- [29] L. Klebl, Z. A. H. Goodwin, A. A. Mostofi, D. M. Kennes, and J. Lischner, Importance of long-ranged electron-electron interactions for the magnetic phase diagram of twisted bilayer graphene, *Phys. Rev. B* **103**, 195127 (2021).
- [30] M. Xie and A. H. MacDonald, Nature of the correlated insulator states in twisted bilayer graphene, *Phys. Rev. Lett.* **124**, 097601 (2020).
- [31] F. M. Faulstich, K. D. Stubbs, Q. Zhu, T. Soejima, R. Dilip, H. Zhai, R. Kim, M. P. Zaletel, G. K.-L. Chan, and L. Lin, Interacting models for twisted bilayer graphene: A quantum chemistry approach, *Phys. Rev. B* **107**, 235123 (2023).
- [32] O. Vafek and J. Kang, Renormalization group study of hidden symmetry in twisted bilayer graphene with coulomb interactions, *Phys. Rev. Lett.* **125**, 257602 (2020).
- [33] B. A. Bernevig, Z.-D. Song, N. Regnault, and B. Lian, Twisted bilayer graphene. iii. interacting hamiltonian and exact symmetries, *Phys. Rev. B* **103**, 205413 (2021).
- [34] B. Lian, Z.-D. Song, N. Regnault, D. K. Efetov, A. Yazdani, and B. A. Bernevig, Twisted bilayer graphene. iv. exact insulator ground states and phase diagram, *Phys. Rev. B* **103**, 205414 (2021).
- [35] K. Seo, V. N. Kotov, and B. Uchoa, Ferromagnetic mott state in twisted graphene bilayers at the magic angle, *Phys. Rev. Lett.* **122**, 246402 (2019).
- [36] Y. H. Kwan, G. Wagner, N. Bultinck, S. H. Simon, E. Berg, and S. A. Parameswaran, Electron-phonon coupling and competing kekulé orders in twisted bilayer graphene (2023), [arXiv:2303.13602](https://arxiv.org/abs/2303.13602) [cond-mat.str-el].
- [37] P. J. Ledwith, E. Khalaf, and A. Vishwanath, Strong coupling theory of magic-angle graphene: A pedagogical introduction, *Annals of Physics* **435**, 168646 (2021), special issue on Philip W. Anderson.
- [38] A. T. Pierce, Y. Xie, J. M. Park, E. Khalaf, S. H. Lee, Y. Cao, D. E. Parker, P. R. Forrester, S. Chen, K. Watanabe, T. Taniguchi, A. Vishwanath, P. Jarillo-Herrero, and A. Yacoby, Unconventional sequence of correlated chern insulators in magic-angle twisted bilayer graphene, *Nature Physics* **17**, 1210 (2021).
- [39] D. E. Parker, T. Soejima, J. Hauschild, M. P. Zaletel, and N. Bultinck, Strain-induced quantum phase transitions in magic-angle graphene, *Phys. Rev. Lett.* **127**, 027601 (2021).
- [40] K. P. Nuckolls, R. L. Lee, M. Oh, D. Wong, T. Soejima, J. P. Hong, D. Călugăru, J. Herzog-Arbeitman, B. A. Bernevig, K. Watanabe, T. Taniguchi, N. Regnault, M. P. Zaletel, and A. Yazdani, Quantum textures of the many-body wavefunctions in magic-angle graphene (2023), [arXiv:2303.00024](https://arxiv.org/abs/2303.00024) [cond-mat.mes-hall].
- [41] D. Călugăru, N. Regnault, M. Oh, K. P. Nuckolls, D. Wong, R. L. Lee, A. Yazdani, O. Vafek, and B. A. Bernevig, Spectroscopy of twisted bilayer graphene correlated insulators, *Phys. Rev. Lett.* **129**, 117602 (2022).
- [42] A. Jimeno-Pozo, Z. A. H. Goodwin, P. A. Pantaleón, V. Vitale, L. Klebl, D. M. Kennes, A. Mostofi, J. Lischner, and F. Guinea, Short vs. long range exchange interactions in twisted bilayer graphene (2023), [arXiv:2303.18025](https://arxiv.org/abs/2303.18025) [cond-mat.mes-hall].
- [43] A. Blason and M. Fabrizio, Local kekulé distortion turns twisted bilayer graphene into topological mott insulators and superconductors, *Phys. Rev. B* **106**, 235112 (2022).
- [44] D. R. Hofstadter, Energy levels and wave functions of bloch electrons in rational and irrational magnetic fields, *Phys. Rev. B* **14**, 2239 (1976).
- [45] J. Herzog-Arbeitman, Z.-D. Song, N. Regnault, and B. A. Bernevig, Hofstadter topology: Noncrystalline topologi-

- cal materials at high flux, *Phys. Rev. Lett.* **125**, 236804 (2020).
- [46] B. Lian, F. Xie, and B. A. Bernevig, Landau level of fragile topology, *Phys. Rev. B* **102**, 041402 (2020).
- [47] Y. Guan, O. V. Yazyev, and A. Kruchkov, Reentrant magic-angle phenomena in twisted bilayer graphene in integer magnetic fluxes, *Phys. Rev. B* **106**, L121115 (2022).
- [48] K. Singh, A. Chew, J. Herzog-Arbeitman, B. A. Bernevig, and O. Vafek, Topological heavy fermions in magnetic field (2023), [arXiv:2305.08171](https://arxiv.org/abs/2305.08171) [cond-mat.str-el].
- [49] X. Wang and O. Vafek, Narrow bands in magnetic field and strong-coupling hofstadter spectra, *Phys. Rev. B* **106**, L121111 (2022).
- [50] J. Herzog-Arbeitman, A. Chew, and B. A. Bernevig, Magnetic bloch theorem and reentrant flat bands in twisted bilayer graphene at 2π flux, *Phys. Rev. B* **106**, 085140 (2022).
- [51] J. Herzog-Arbeitman, A. Chew, D. K. Efetov, and B. A. Bernevig, Reentrant correlated insulators in twisted bilayer graphene at $25t$ (2π flux), *Phys. Rev. Lett.* **129**, 076401 (2022).
- [52] I. Das, C. Shen, A. Jaoui, J. Herzog-Arbeitman, A. Chew, C.-W. Cho, K. Watanabe, T. Taniguchi, B. A. Piot, B. A. Bernevig, and D. K. Efetov, Observation of reentrant correlated insulators and interaction-driven fermi-surface reconstructions at one magnetic flux quantum per moiré unit cell in magic-angle twisted bilayer graphene, *Phys. Rev. Lett.* **128**, 217701 (2022).
- [53] R. Bistritzer and A. H. MacDonald, Moiré bands in twisted double-layer graphene, *Proceedings of the National Academy of Sciences* **108**, 12233 (2011), <https://www.pnas.org/doi/pdf/10.1073/pnas.1108174108>.
- [54] J. M. B. Lopes dos Santos, N. M. R. Peres, and A. H. Castro Neto, Continuum model of the twisted graphene bilayer, *Phys. Rev. B* **86**, 155449 (2012).
- [55] Z. A. H. Goodwin, V. Vitale, X. Liang, A. A. Mostofi, and J. Lischner, Hartree theory calculations of quasiparticle properties in twisted bilayer graphene, *Electronic Structure* **2**, 034001 (2020).
- [56] J. Kang and O. Vafek, Pseudomagnetic fields, particle-hole asymmetry, and microscopic effective continuum hamiltonians of twisted bilayer graphene, *Phys. Rev. B* **107**, 075408 (2023).
- [57] N. N. T. Nam and M. Koshino, Lattice relaxation and energy band modulation in twisted bilayer graphene, *Phys. Rev. B* **96**, 075311 (2017).
- [58] P. Moon and M. Koshino, Energy spectrum and quantum hall effect in twisted bilayer graphene, *Phys. Rev. B* **85**, 195458 (2012).
- [59] G. Giuliani and G. Vignale, *Quantum Theory of the Electron Liquid* (Cambridge University Press, 2005).
- [60] J. M. Luttinger, The effect of a magnetic field on electrons in a periodic potential, *Phys. Rev.* **84**, 814 (1951).
- [61] N. Nemeč and G. Cuniberti, Hofstadter butterflies of bilayer graphene, *Phys. Rev. B* **75**, 201404 (2007).
- [62] J. Herzog-Arbeitman, Z.-D. Song, L. Elcoro, and B. A. Bernevig, [Hofstadter topology with real space invariants and reentrant projective symmetries](#) (2022).
- [63] J. Ahn, S. Park, and B.-J. Yang, Failure of nielsen-ninomiya theorem and fragile topology in two-dimensional systems with space-time inversion symmetry: Application to twisted bilayer graphene at magic angle, *Phys. Rev. X* **9**, 021013 (2019).
- [64] T. Fukui, Y. Hatsugai, and H. Suzuki, Chern numbers in discretized brillouin zone: Efficient method of computing (spin) hall conductances, *Journal of the Physical Society of Japan* **74**, 1674 (2005), <https://doi.org/10.1143/JPSJ.74.1674>.
- [65] Z.-D. Song, B. Lian, N. Regnault, and B. A. Bernevig, Twisted bilayer graphene. ii. stable symmetry anomaly, *Phys. Rev. B* **103**, 205412 (2021).
- [66] G. Tarnopolsky, A. J. Kruchkov, and A. Vishwanath, Origin of magic angles in twisted bilayer graphene, *Phys. Rev. Lett.* **122**, 106405 (2019).
- [67] J. Liu, J. Liu, and X. Dai, Pseudo landau level representation of twisted bilayer graphene: Band topology and implications on the correlated insulating phase, *Phys. Rev. B* **99**, 155415 (2019).
- [68] S. Chatterjee, N. Bultinck, and M. P. Zaletel, Symmetry breaking and skyrmionic transport in twisted bilayer graphene, *Phys. Rev. B* **101**, 165141 (2020).
- [69] J. González and T. Stauber, Ising superconductivity induced from spin-selective valley symmetry breaking in twisted trilayer graphene, *Nature Communications* **14**, 2746 (2023).
- [70] T. Cea, P. A. Pantaleón, N. R. Walet, and F. Guinea, Electrostatic interactions in twisted bilayer graphene, *Nano Materials Science* **4**, 27 (2022), special issue on Graphene and 2D Alternative Materials.
- [71] M. S. Scheurer and R. Samajdar, Pairing in graphene-based moiré superlattices, *Phys. Rev. Res.* **2**, 033062 (2020).
- [72] S. Chatterjee, T. Wang, E. Berg, and M. P. Zaletel, Intervalley coherent order and isospin fluctuation mediated superconductivity in rhombohedral trilayer graphene, *Nature Communications* **13**, 6013 (2022).
- [73] J. Y. Lee, E. Khalaf, S. Liu, X. Liu, Z. Hao, P. Kim, and A. Vishwanath, Theory of correlated insulating behaviour and spin-triplet superconductivity in twisted double bilayer graphene, *Nature Communications* **10**, 5333 (2019).
- [74] C. Chen, K. P. Nuckolls, S. Ding, W. Miao, D. Wong, M. Oh, R. L. Lee, S. He, C. Peng, D. Pei, Y. Li, S. Zhang, J. Liu, Z. Liu, C. Jozwiak, A. Bostwick, E. Rotenberg, C. Li, X. Han, D. Pan, X. Dai, C. Liu, B. A. Bernevig, Y. Wang, A. Yazdani, and Y. Chen, Strong inter-valley electron-phonon coupling in magic-angle twisted bilayer graphene (2023), [arXiv:2303.14903](https://arxiv.org/abs/2303.14903) [cond-mat.mes-hall].
- [75] Z. A. H. Goodwin, F. Corsetti, A. A. Mostofi, and J. Lischner, Attractive electron-electron interactions from internal screening in magic-angle twisted bilayer graphene, *Phys. Rev. B* **100**, 235424 (2019).
- [76] A. Ramires and J. L. Lado, Impurity-induced triple point fermions in twisted bilayer graphene, *Phys. Rev. B* **99**, 245118 (2019).

Appendix A: The symmetry operations under magnetic fields

We look for unitary operators realizing the C_{3z} and C_{2z} symmetries, acting on the creation operators as

$$g c_{\mathbf{i}}^\dagger g^{-1} = \exp(i\chi_g(g(\mathbf{r}_{\mathbf{i}}))) c_{g(\mathbf{i})}^\dagger. \quad (\text{A1})$$

Here we use indistinctly g for the unitary operators and for the linear transformations acting on points of the lattice. These can always be distinguished by the context. As in the main text, $c_{\mathbf{i}}^\dagger (c_{g(\mathbf{i})}^\dagger)$ is the creation operator at position $\mathbf{r}_{\mathbf{i}}$ ($g(\mathbf{r}_{\mathbf{i}})$). The action on the Hamiltonian is

$$g H_0 g^{-1} = \sum_{\mathbf{i}, \mathbf{j}} t(\mathbf{r}_{\mathbf{i}} - \mathbf{r}_{\mathbf{j}}) \exp(i\theta_{\mathbf{i}, \mathbf{j}}) \exp(i(\chi_g(g(\mathbf{r}_{\mathbf{i}})) - \chi_g(g(\mathbf{r}_{\mathbf{j}})))) c_{g(\mathbf{i})}^\dagger c_{g(\mathbf{j})}. \quad (\text{A2})$$

We are dealing with symmetries at zero flux, so $t(g(\mathbf{r}_{\mathbf{i}}) - g(\mathbf{r}_{\mathbf{j}})) = t(\mathbf{r}_{\mathbf{i}} - \mathbf{r}_{\mathbf{j}})$. Then to realize the symmetry (this is, for $g H_0 g^{-1} = H_0$) $\chi_g(\mathbf{r})$ must obey

$$\begin{aligned} \theta_{g^{-1}(\mathbf{i}), g^{-1}(\mathbf{j})} + \chi_g(\mathbf{r}_{\mathbf{i}}) - \chi_g(\mathbf{r}_{\mathbf{j}}) &= \theta_{\mathbf{i}, \mathbf{j}} \\ \frac{2\pi}{\Phi_0} \int_{g^{-1}(\mathbf{r}_{\mathbf{i}})}^{g^{-1}(\mathbf{r}_{\mathbf{j}})} \mathbf{A}(\mathbf{r}') \cdot d\mathbf{r}' - \frac{2\pi}{\Phi_0} \int_{\mathbf{r}_{\mathbf{i}}}^{\mathbf{r}_{\mathbf{j}}} \mathbf{A}(\mathbf{r}') \cdot d\mathbf{r}' &= \int_{\mathbf{r}_{\mathbf{i}}}^{\mathbf{r}_{\mathbf{j}}} \nabla \chi_g(\mathbf{r}') \cdot d\mathbf{r}' \\ \frac{2\pi}{\Phi_0} \left(g(\mathbf{A}(g^{-1}(\mathbf{r}))) - \mathbf{A}(\mathbf{r}) \right) &= \nabla \chi_g(\mathbf{r}). \end{aligned} \quad (\text{A3})$$

In the periodic Landau gauge $\mathbf{A}(\mathbf{r}) = \frac{\Phi}{2\pi} \left(\xi_1 \mathbf{G}_2 - 2\pi \nabla (\xi_2 [\xi_1 + \epsilon]) \right)$ where ξ_1 and ξ_2 are defined by $\mathbf{r} = \xi_1 \mathbf{L}_1 + \xi_2 \mathbf{L}_2$.

We have for C_{3z}

$$C_{3z}(\mathbf{A}(C_{3z}^{-1}(\mathbf{r}))) = \frac{\Phi}{2\pi} \left(-\xi_2 (\mathbf{G}_2 - \mathbf{G}_1) + 2\pi \nabla \left((\xi_2 + \xi_1) [\xi_2 + \epsilon] \right) \right), \quad (\text{A4})$$

and hence

$$\chi_{C_{3z}}(\mathbf{r}) = \frac{2\pi p}{q} \left((\xi_1 + \xi_2) [\xi_2 + \epsilon] + \xi_2 [\xi_1 + \epsilon] - \xi_1 \xi_2 - \frac{\xi_2^2}{2} \right). \quad (\text{A5})$$

Similarly for C_{2z} we get

$$\begin{aligned} C_{2z}(\mathbf{A}(C_{2z}^{-1}(\mathbf{r}))) &= \frac{\Phi}{2\pi} \left(\xi_1 \mathbf{G}_2 + 2\pi \nabla \left(\xi_2 [-\xi_1 + \epsilon] \right) \right), \\ \chi_{C_{2z}}(\mathbf{r}) &= \frac{2\pi p}{q} \left(\xi_2 [\xi_1 + \epsilon] + \xi_2 [-\xi_1 + \epsilon] \right). \end{aligned} \quad (\text{A6})$$

Above we have used the facts that for orthogonal transformations g and scalar functions $f(\mathbf{r})$ and $h(\mathbf{r}) = f(g^{-1}(\mathbf{r}))$, we have $\nabla h|_{\mathbf{r}} = g(\nabla f|_{g^{-1}(\mathbf{r})})$, and that for a function of ξ_1 and ξ_2 we have $2\pi \nabla f = \frac{\partial f}{\partial \xi_1} \mathbf{G}_1 + \frac{\partial f}{\partial \xi_2} \mathbf{G}_2$. The functions $\chi_{C_{3z}}$ and $\chi_{C_{2z}}$ have the following periodicity properties

$$\begin{aligned} \chi_{C_{3z}}(\mathbf{r} + q\mathbf{L}_2) &= \chi_{C_{3z}}(\mathbf{r}) + \pi p q \text{ mod } 2\pi, & \chi_{C_{3z}}(\mathbf{r} + \mathbf{L}_1) &= \chi_{C_{3z}}(\mathbf{r}) + \frac{2\pi p}{q} [\xi_2 + \epsilon] \\ \chi_{C_{2z}}(\mathbf{r} + q\mathbf{L}_2) &= \chi_{C_{2z}}(\mathbf{r}) \text{ mod } 2\pi, & \chi_{C_{2z}}(\mathbf{r} + \mathbf{L}_1) &= \chi_{C_{2z}}(\mathbf{r}). \end{aligned} \quad (\text{A7})$$

We are interested in $p = q = 1$, so we can write

$$\begin{aligned} e^{i\chi_{C_{3z}}(\mathbf{r})} &= e^{-i\mathbf{G}_2 \cdot \mathbf{r}/2} e^{i\bar{\chi}_{C_{3z}}(\mathbf{r})} \\ e^{i\chi_{C_{2z}}(\mathbf{r})} &= e^{i\bar{\chi}_{C_{2z}}(\mathbf{r})}, \end{aligned} \quad (\text{A8})$$

where barred phases are periodic in the Moiré unit cell. As we will see now, the phases $e^{i\chi_{C_{3z}}(\mathbf{r})}$ and $e^{i\chi_{C_{2z}}(\mathbf{r})}$ modify the transformations of the Bloch waves, redefining the high symmetry points in flux.

The Bloch waves are written

$$c_{\mathbf{k},i}^\dagger = \frac{1}{\sqrt{N_M}} \sum_{\mathbf{l}} e^{i\mathbf{k}\cdot(\mathbf{R}_l + \boldsymbol{\delta}_i)} c_{\mathbf{l},i}^\dagger, \quad (\text{A9})$$

with \mathbf{k} belonging to the Moiré Brillouin zone, and here $c_{\mathbf{l},i}^\dagger$ creates an electron at position $\mathbf{R}_l + \boldsymbol{\delta}_i$ where \mathbf{R}_l is a lattice vector and $\boldsymbol{\delta}_i$ belongs to the Wigner-Seitz cell.

Under C_{3z} , $c_{\mathbf{k},i}^\dagger$ transforms as

$$C_{3z} c_{\mathbf{k},i}^\dagger (C_{3z})^{-1} = \frac{1}{\sqrt{N_M}} \sum_{\mathbf{l}} e^{i(C_{3z}(\mathbf{k}) - \mathbf{G}_2/2) \cdot C_{3z}(\mathbf{R}_l + \boldsymbol{\delta}_i)} e^{i\bar{\chi}_{C_{3z}}(C_{3z}(\boldsymbol{\delta}_i))} c_{C_{3z}(\mathbf{l},i)}^\dagger. \quad (\text{A10})$$

Here, $c_{C_{3z}(\mathbf{l},i)}^\dagger$ creates an electron at position $C_{3z}(\mathbf{R}_l + \boldsymbol{\delta}_i)$. We see that C_{3z} sends momentum \mathbf{k} to $C_{3z}(\mathbf{k}) - \mathbf{G}_2/2$. Via the embedding relation $c_{\mathbf{k}+\mathbf{G},i}^\dagger = e^{i\mathbf{G}\cdot\boldsymbol{\delta}_i} c_{\mathbf{k},i}^\dagger$ for \mathbf{G} a reciprocal lattice vector, the three-fold rotation in flux acts in the momenta as follows,

$$\mathbf{k} \xrightarrow{C_{3z}} C_{3z}(\mathbf{k}) - \mathbf{G}_2/2 \sim C_{3z}\left(\mathbf{k} - (\mathbf{G}_1 + \mathbf{G}_2)/2\right) + (\mathbf{G}_1 + \mathbf{G}_2)/2. \quad (\text{A11})$$

Also, given that $\chi_{C_{2z}}(\mathbf{r})$ is periodic mod 2π on the unit cell, the momentum transforms like in zero flux,

$$\mathbf{k} \xrightarrow{C_{2z}} C_{2z}(\mathbf{k}) \sim C_{2z}\left(\mathbf{k} - (\mathbf{G}_1 + \mathbf{G}_2)/2\right) + (\mathbf{G}_1 + \mathbf{G}_2)/2. \quad (\text{A12})$$

The center of rotations has shifted from $\boldsymbol{\Gamma}_M$ to one of the other parity invariant points, $(\mathbf{G}_1 + \mathbf{G}_2)/2$, at one magnetic flux quantum.

Now we look for the operator realizing C_{2y} . The procedure is the same, but in this case $C_{2y}H_0(C_{2y})^{-1}$ should be equal to the Hamiltonian with the sign of the magnetic field reversed. Hence, $\chi_{C_{2y}}(\mathbf{r})$ must obey

$$C_{2y}(\mathbf{A}(C_{2y}^{-1}(\mathbf{r}))) + \mathbf{A}(\mathbf{r}) = \nabla \chi_{C_{2y}}(\mathbf{r}). \quad (\text{A13})$$

We obtain for $\chi_{C_{2y}}(\mathbf{r})$

$$\chi_{C_{2y}}(\mathbf{r}) = \frac{2\pi p}{q} \left(-\xi_2[\xi_1 + \epsilon] + \xi_2[\xi_1 + \xi_2 + \epsilon] - \frac{\xi_2^2}{2} \right), \quad (\text{A14})$$

which obeys the properties

$$\chi_{C_{2y}}(\mathbf{r} + q\mathbf{L}_2) = \chi_{C_{2y}}(\mathbf{r}) - \pi pq \text{ mod } 2\pi, \quad \chi_{C_{2y}}(\mathbf{r} + \mathbf{L}_1) = \chi_{C_{2y}}(\mathbf{r}). \quad (\text{A15})$$

The same analysis as before applies, and under C_{2y} the momentum transform as

$$\mathbf{k} \xrightarrow{C_{2y}} C_{2y}(\mathbf{k}) - \mathbf{G}_2/2 \sim C_{2y}\left(\mathbf{k} - (\mathbf{G}_1 + \mathbf{G}_2)/2\right) + (\mathbf{G}_1 + \mathbf{G}_2)/2. \quad (\text{A16})$$

For the time reversal operator \mathcal{T} , the magnetic field should be reversed also, and it is trivial to see that the action is the same as for the zero flux case. \mathcal{T} is an antiunitary operator satisfying $\mathcal{T}c_i^\dagger\mathcal{T}^{-1} = c_i^\dagger$, and transforming the momentum as

$$\mathbf{k} \xrightarrow{\mathcal{T}} -\mathbf{k} \sim -\left(\mathbf{k} - (\mathbf{G}_1 + \mathbf{G}_2)/2\right) + (\mathbf{G}_1 + \mathbf{G}_2)/2. \quad (\text{A17})$$

In conclusion, the action of symmetry operators under one magnetic flux quantum effectively shift the Brillouin zone by $(\mathbf{G}_1 + \mathbf{G}_2)/2$, redefining the high symmetry points.

Appendix B: Valley charge and $C_{2z}P$ operator on the lattice

We wish to find an operator τ_z implementing the valley charge on the lattice, such that $\langle \tau_z \rangle = +1$ on states nearby the K point of graphene and -1 near the K' point. We adopt a slight generalization of the valley operator of Ref. [76]

$$\tau_z = \frac{i}{3\sqrt{3}} \sum_l \left(\sum_{\nabla} e^{-i\theta_{\nabla(1),\nabla(2)}} c_{\nabla(1)}^\dagger c_{\nabla(2)} + e^{-i\theta_{\nabla(2),\nabla(3)}} c_{\nabla(2)}^\dagger c_{\nabla(3)} + e^{-i\theta_{\nabla(3),\nabla(1)}} c_{\nabla(3)}^\dagger c_{\nabla(1)} - \sum_{\Delta} e^{-i\theta_{\Delta(1),\Delta(2)}} c_{\Delta(1)}^\dagger c_{\Delta(2)} + e^{-i\theta_{\Delta(2),\Delta(3)}} c_{\Delta(2)}^\dagger c_{\Delta(3)} + e^{-i\theta_{\Delta(3),\Delta(1)}} c_{\Delta(3)}^\dagger c_{\Delta(1)} \right) + \text{h.c.} \quad (\text{B1})$$

The sums are over triangles upside down of sublattice A atoms, and triangles of sublattice B , and l denotes the sum over the two layers. We draw an example of each kind of triangle in Figure C.3. The phases are the Peierls' phases defined in the main text. It can be shown that valley K states have $\langle \tau_z \rangle = +1 + O(a/L_M)$ and valley K' states have $\langle \tau_z \rangle = -1 + O(a/L_M)$.

For the particle-hole operator $C_{2z}P$ (Eq.11) we proceed as follows. Once we have valley polarized states, we obtain the envelope functions $\Psi_{\eta\sigma l}$ by multiplying Ψ_η with the valley factor $e^{-i\eta n_\theta \mathbf{G}_2 \cdot \mathbf{r}}$. Afterwards, we perform a smooth interpolation of the data $\Psi_{\eta\sigma l}(\mathbf{r}_i)$ being \mathbf{r}_i the positions of the atoms at sublattice σ and layer l . Finally, the smooth functions are sampled at the points of the opposite sublattice and layer, and the factor $\eta_{s'l} e^{-i\eta n_\theta \mathbf{G}_2 \cdot \mathbf{r}} e^{-i\eta \mathbf{G}_2 \cdot \mathbf{r}}$ is also added. As a note, When $\Phi = \Phi_0$ the envelopes have a discontinuity at $\xi_1 =$ an integer in the periodic Landau gauge, and special care is needed when performing the interpolation.

The projected operator in the flat bands $[\overline{C_{2z}P}(\mathbf{k})]_{\rho\rho'} = \langle \mathbf{k}\rho | C_{2z}P | \mathbf{k}\rho' \rangle = \langle \mathbf{k}\rho | C_{2z}P(\mathbf{k}\rho') \rangle$ is then constructed. We have checked that the particular choice of basis for the interpolation is irrelevant, and the matrix elements of $\overline{C_{2z}P}(\mathbf{k})$ in a different basis computed via interpolation or unitary conjugation of the original matrix are essentially identical.

In order to check the validity of our definitions, we have computed several benchmarks. The mean of the absolute value of the matrix elements of $\overline{C_{2z}P}(\mathbf{k}) - \overline{C_{2z}P}(\mathbf{k})^\dagger$ are always less than 10^{-5} , so we capture well the hermiticity of $C_{2z}P$. Also, the mean of the absolute value of the valley off-diagonal matrix elements of $\overline{C_{2z}P}(\mathbf{k})$ are always less than 10^{-5} for Φ_0 flux and 10^{-7} at zero field. We conclude that our implementations of the valley charge and the p-h operator are trustworthy.

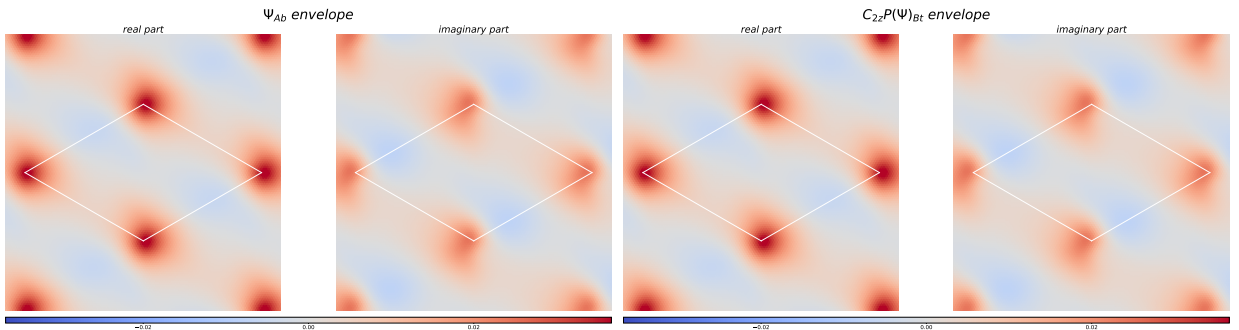


FIG. B.1: $C_{2z}P$ operator at zero flux. **Left:** for the state $|M_M K A\rangle$ at zero field we plot the smooth envelope at sublattice A bottom layer, $\Psi_{KAb}(\mathbf{r})$. **Right:** for the $C_{2z}P$ transformed state, we plot $e^{i\eta n_\theta \mathbf{G}_2 \cdot \mathbf{r}} e^{i\mathbf{G}_2 \cdot \mathbf{r}} C_{2z}P(\Psi_K)_{Bt}(\mathbf{r})$.

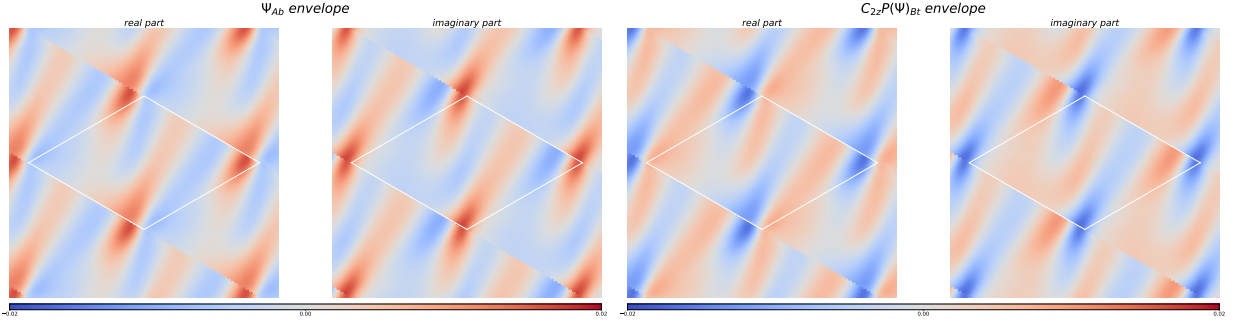


FIG. B.2: $C_{2z}P$ operator at one flux quantum. In this case we plot the envelope of $|M_M K' + 1\rangle$ at 26.5 T in the right, and $e^{-in_\theta \mathbf{G}_2 \cdot \mathbf{r}} e^{-i\mathbf{G}_2 \cdot \mathbf{r}} C_{2z}P(\Psi'_K)_{Bt}(\mathbf{r})$ in the left plot. Notice the discontinuities of the wave function on the unit cell edge due to the periodic Landau gauge, and the extra minus sign $\eta = -1$ in the transformed wave function, see Eq. 11.

Appendix C: $U(1)_v$ AND $SU(2)_K \times SU(2)_{K'}$ symmetries in the lattice model

In the BM model, a general wave function can be written similarly to Eq. 10, in a 4 component notation for sublattice and layer (t =top, b =bottom),

$$u(\mathbf{r}) = e^{i\mathbf{K}_u \cdot \mathbf{r}} (u_{At}(\mathbf{r}), u_{Bt}(\mathbf{r}), u_{Ab}(\mathbf{r}), u_{Bb}(\mathbf{r}))^T, \quad (C1)$$

with $\mathbf{K}_u = \pm \mathbf{K}$, the graphene Dirac points, and the envelope functions are smooth on the graphene scale. The matrix elements of the Coulomb interaction (actually, the four fermion part of the normal ordered operator) read

$$\langle ab|V|cd\rangle = \frac{1}{2} \sum_{\{\sigma\}, \{\iota\}} \int d\mathbf{r}_i \int d\mathbf{r}_j V(\mathbf{r}_i - \mathbf{r}_j) e^{i(\mathbf{K}_c - \mathbf{K}_a) \cdot \mathbf{r}_i} e^{i(\mathbf{K}_d - \mathbf{K}_b) \cdot \mathbf{r}_j} a_{\sigma_a l_a}^*(\mathbf{r}_i) b_{\sigma_b l_b}^*(\mathbf{r}_j) c_{\sigma_c l_c}(\mathbf{r}_i) d_{\sigma_d l_d}(\mathbf{r}_j). \quad (C2)$$

This integral computes the Fourier transform of the potential at momenta $\sim \mathbf{K}_a - \mathbf{K}_c$, or equivalently $\sim \mathbf{K}_d - \mathbf{K}_b$. Hence, unless $\mathbf{K}_a = \mathbf{K}_c$ and $\mathbf{K}_b = \mathbf{K}_d$ the form factor is negligible given $\|\mathbf{K}\| \sim a^{-1} \gg \xi^{-1}$. This is the origin of $U(1)_v$ and $SU(2)_K \times SU(2)_{K'}$ in TBG.

In the tight-binding, we write states $|u\rangle$, with wavefunctions

$$\langle \mathbf{r}_i | u \rangle = e^{i\mathbf{K}_u \cdot \mathbf{r}_i} u(\mathbf{r}_i). \quad (C3)$$

$u(\mathbf{r}_i)$ is further decomposed depending on the sublattice and layer of the point \mathbf{r}_i , $u(\mathbf{r}_i) = \sum_{\sigma l} u_{\sigma l}(\mathbf{r}_i) \delta_{\mathbf{r}_i \in \sigma l}$. The functions $u_{\sigma l}(\mathbf{r}_i)$ vary slowly on the graphene scale, such that $u_{\sigma l}(\mathbf{r}_i + \mathbf{a}_{1,2}) \approx u_{\sigma l}(\mathbf{r}_i)$. Consider the matrix element of the interaction (actually, the four fermion part of the normal ordered operator)

$$\langle ab|V|cd\rangle = \frac{1}{2} \sum_{\mathbf{r}_i, \mathbf{r}_j} V(\mathbf{r}_i - \mathbf{r}_j) e^{-i(\mathbf{K}_a - \mathbf{K}_c) \cdot \mathbf{r}_i} e^{-i(\mathbf{K}_b - \mathbf{K}_d) \cdot \mathbf{r}_j} a^*(\mathbf{r}_i) b^*(\mathbf{r}_j) c(\mathbf{r}_i) d(\mathbf{r}_j) \quad (C4)$$

We will see that if the valley charge is not conserved, i.e. $\mathbf{K}_a + \mathbf{K}_b - \mathbf{K}_c - \mathbf{K}_d \neq \mathbf{0}$ the matrix element vanishes to a first approximation. Let us take for example $\mathbf{K}_a = \mathbf{K}_c = \mathbf{K}_d = -\mathbf{K}_b = \mathbf{K}$, then

$$\langle ab|V|cd\rangle = \frac{1}{2} \sum_{\mathbf{r}_i, \mathbf{r}_j} V(\mathbf{r}_i - \mathbf{r}_j) e^{-2i\mathbf{K} \cdot \mathbf{r}_i} a^*(\mathbf{r}_i) b^*(\mathbf{r}_j) c(\mathbf{r}_i) d(\mathbf{r}_j). \quad (C5)$$

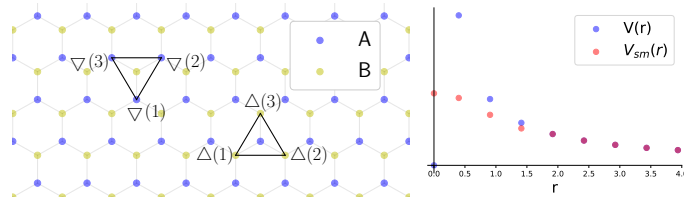


FIG. C.3: **Left:** Triangular loops that calculate the valley charge. **Right:** Decomposition of the potential. $V_{sm}(r)$ is a smoothed version of $V(r)$

Shifting the integration variables $\mathbf{r}_{i,j} \rightarrow \mathbf{r}_{i,j} + \mathbf{a}_1$ and using the property of the envelope functions $u(\mathbf{r}_i + \mathbf{a}_{1,2}) \approx u(\mathbf{r}_i)$ we get

$$\langle ab|V|cd \rangle = e^{-2i\mathbf{K}\cdot\mathbf{a}_1} \langle ab|V|cd \rangle = e^{-2\pi i/3} \langle ab|V|cd \rangle = 0. \quad (\text{C6})$$

The argument for other charge non conserving combinations of $\mathbf{K}_{\mathbf{a},\mathbf{b},\mathbf{c},\mathbf{d}}$ is the same and we conclude that $U(1)_v$ is a symmetry in the atomistic model also.

If $\mathbf{K}_{\mathbf{a}} = \mathbf{K}_{\mathbf{d}} = -\mathbf{K}_{\mathbf{b}} = -\mathbf{K}_{\mathbf{c}}$, say $\mathbf{K}_{\mathbf{a}} = \mathbf{K}$, we have

$$\langle ab|V|cd \rangle = \frac{1}{2} \sum_{\mathbf{r}_i, \mathbf{r}_j} V(\mathbf{r}_i - \mathbf{r}_j) e^{-2i\mathbf{K}\cdot(\mathbf{r}_i - \mathbf{r}_j)} a^*(\mathbf{r}_i) b^*(\mathbf{r}_j) c(\mathbf{r}_i) d(\mathbf{r}_j), \quad (\text{C7})$$

and the shifting argument does not work because the phases for \mathbf{r}_i and \mathbf{r}_j cancel. In general these matrix elements are non zero and break the $SU(2)_K \times SU(2)_{K'}$ symmetry of independent spin rotations in each valley.

Furthermore, the exchange energy of states with different valley charge, say $|a\rangle = |d\rangle$ and $|b\rangle = |c\rangle$, is always positive. For that, decompose the potential into a smooth part $V_{sm}(\mathbf{r})$ and a short-range part $V_{sr}(\mathbf{r})$. $V_{sm}(\mathbf{r})$ is slowly varying on the graphene scale, is equal to $V(\mathbf{r})$ at long distances (say $\|\mathbf{r}\| > 2a$) and $V_{sm}(\mathbf{0})$ equals a positive constant. On the other hand, $V_{sr}(\mathbf{r}) = V(\mathbf{r}) - V_{sm}(\mathbf{r})$ is equal to $-V_{sm}(\mathbf{0})$ at $\mathbf{r} = \mathbf{0}$ (remember the on-site interaction is treated separately by the Hubbard term, so $V(\mathbf{0}) = 0$), exhibits the steep Coulomb repulsion at short distances and vanishes at long distances. In Fig. C.3 we sketch this decomposition.

Given that $V_{sm}(\mathbf{r} + \mathbf{a}_{1,2}) \approx V_{sm}(\mathbf{r})$, one can apply the shifting only to the first variable \mathbf{r}_i , and get

$$\langle ab|V_{sm}|ba \rangle = e^{-2i\mathbf{K}\cdot\mathbf{a}_1} \langle ab|V_{sm}|ba \rangle = e^{-2\pi i/3} \langle ab|V_{sm}|ba \rangle = 0. \quad (\text{C8})$$

For $V_{sr}(\mathbf{r})$ let us consider only the dominant contributions of intralayer terms with $\|\mathbf{r}_i - \mathbf{r}_j\| = 0, a_0$ and a .

$$\begin{aligned} \langle ab|V_{sr}|ba \rangle &= \frac{1}{2} \sum_{\mathbf{r}_j} V_0 |a_{\sigma_j l_j}(\mathbf{r}_j)|^2 |b_{\sigma_j l_j}(\mathbf{r}_j)|^2 + 3V_a (e^{2\pi i/3} + e^{-2\pi i/3}) |a_{\sigma_j l_j}(\mathbf{r}_j)|^2 |b_{\sigma_j l_j}(\mathbf{r}_j)|^2 \\ &\quad + V_{a_0} (1 + e^{2\pi i/3} + e^{-2\pi i/3}) a_{\bar{\sigma}_j l_j}^*(\mathbf{r}_j) a_{\sigma_j l_j}(\mathbf{r}_j) b_{\sigma_j l_j}^*(\mathbf{r}_j) b_{\bar{\sigma}_j l_j}(\mathbf{r}_j) \\ &= \frac{1}{2} \sum_{\mathbf{r}_j} (V_0 - 3V_a) |a(\mathbf{r}_j)|^2 |b(\mathbf{r}_j)|^2 < 0, \end{aligned} \quad (\text{C9})$$

σ_j and l_j denoting the sublattice and layer of the point \mathbf{r}_j and $\bar{\sigma}_j$ the opposite sublattice to σ_j . V_r encodes the value of $V_{sr}(\mathbf{r})$ when $\|\mathbf{r}\| = r$. Notice that $V_0 < 0$ and $V_a > 0$. In turn, the exchange energy $-\langle ab|V|ba \rangle$ is always positive

Appendix D: The Hartree-Fock method and flat band projection

Consider the normal ordered interaction of Eqs. 5 and 6,

$$V + H_U = \frac{1}{2} \sum_{\mathbf{r}_i, \mathbf{r}_j, s_i, s_j} V(\mathbf{r}_i - \mathbf{r}_j) : c_{i, s_i}^\dagger c_{i, s_i} c_{j, s_j}^\dagger c_{j, s_j} : + U \sum_{\mathbf{i}} : c_{i\uparrow}^\dagger c_{\mathbf{i}\uparrow} c_{i\downarrow}^\dagger c_{i\downarrow} : \quad (\text{D1})$$

The choice of the normal ordering with respect to the ground state of graphene at charge neutrality is necessary to avoid double counting the interaction[21, 30]. This is, we assume that the hopping integrals $t(\mathbf{r})$ are already renormalized by the interactions with the deep Fermi sea of graphene. After expanding the normal ordered product[59] and performing the Hartree-Fock decoupling, the Hamiltonian reads

$$\begin{aligned} V_{\text{HF}} + H_{\text{UHF}} &= \sum_{\mathbf{r}_i, \mathbf{r}_j, s_i, s_j} V(\mathbf{r}_i - \mathbf{r}_j) c_{i s_i}^\dagger c_{i s_i} \left(\langle c_{j s_j}^\dagger c_{j s_j} \rangle - \langle c_{j s_j}^\dagger c_{j s_j} \rangle_0 \right) - \sum_{\mathbf{r}_i, \mathbf{r}_j, s} V(\mathbf{r}_i - \mathbf{r}_j) c_{i s}^\dagger c_{j s} \left(\langle c_{i s}^\dagger c_{j s} \rangle - \langle c_{i s}^\dagger c_{j s} \rangle_0 \right)^* \\ &\quad + U \sum_{\mathbf{r}_i} c_{i\uparrow}^\dagger c_{i\uparrow} \left(\langle c_{i\downarrow}^\dagger c_{i\downarrow} \rangle - \langle c_{i\downarrow}^\dagger c_{i\downarrow} \rangle_0 \right) + U \sum_{\mathbf{r}_i} c_{i\downarrow}^\dagger c_{i\downarrow} \left(\langle c_{i\uparrow}^\dagger c_{i\uparrow} \rangle - \langle c_{i\uparrow}^\dagger c_{i\uparrow} \rangle_0 \right) + \text{constant}, \end{aligned} \quad (\text{D2})$$

with $\langle \dots \rangle_0$ denoting the expectation value in the ground state of graphene at charge neutrality, and $\langle \dots \rangle$ the expectation value in the particular state of our Hartree-Fock decoupling. In our implementation we restrict the wave function to be a direct product of spin up and down electrons, such that $\langle c_{i\uparrow}^\dagger c_{j\downarrow} \rangle = 0$ for all $\mathbf{r}_i, \mathbf{r}_j$.

In the projected limit we assume that the remote bands are filled and the relevant physics takes place in the flat bands. In this spirit we compute mean field interaction restricted to the subspace of the flat bands,

$$[V_{\text{HF,p}}(\mathbf{k}, \mathbf{k}') + H_{U\text{HF,p}}(\mathbf{k}, \mathbf{k}')]_{\rho\rho'} = \left(\langle \text{FS} | \otimes \langle \mathbf{k}\rho | \right) \left(V_{\text{HF}} + H_{U\text{HF}} \right) \left(| \text{FS} \rangle \otimes | \mathbf{k}'\rho' \rangle \right), \quad (\text{D3})$$

with $| \text{FS} \rangle \otimes | \mathbf{k}\rho \rangle$ denoting the direct product of the state with the filled remote bands and the state with momentum \mathbf{k} and multi-index ρ . We further assume translational symmetry that makes the mean field Hamiltonian block-diagonal in momentum space, $V_{\text{HF,p}}(\mathbf{k}, \mathbf{k}') + H_{U\text{HF,p}}(\mathbf{k}, \mathbf{k}') = \left(V_{\text{HF,p}}(\mathbf{k}) + H_{U\text{HF,p}}(\mathbf{k}) \right) \delta_{\mathbf{k}, \mathbf{k}'}$.

The self-consistent method starts by proposing an ansatz for the ground state at any given filling, computing the mean field Hamiltonian and performing the flat band projection. Next, we solve the projected mean field Hamiltonian

$$H_{\text{HF,p}}(\mathbf{k}, \mathbf{k}') = \left(H_{0,\text{p}}(\mathbf{k}) + V_{\text{HF,p}}(\mathbf{k}) + H_{U\text{HF,p}}(\mathbf{k}) \right) \delta_{\mathbf{k}, \mathbf{k}'}, \quad (\text{D4})$$

with $H_{0,\text{p}}(\mathbf{k})\delta_{\mathbf{k}, \mathbf{k}'}$ the projected kinetic energy operator. The ground state of this Hamiltonian is then a new ansatz for the self-consistent ground state and the process is repeated until convergence is reached.

The energy of the self-consistent state is

$$\begin{aligned} \langle H \rangle &= \langle V \rangle + \langle H_U \rangle + \langle H_0 \rangle \\ &= \frac{1}{2} \sum_{\mathbf{r}_i, \mathbf{r}_j, s_i, s_j} V(\mathbf{r}_i - \mathbf{r}_j) \left(\langle c_{i s_i}^\dagger c_{i s_i} \rangle - \langle c_{i s_i}^\dagger c_{i s_i} \rangle_0 \right) \left(\langle c_{j s_j}^\dagger c_{j s_j} \rangle - \langle c_{j s_j}^\dagger c_{j s_j} \rangle_0 \right) - \frac{1}{2} \sum_{\mathbf{r}_i, \mathbf{r}_j, s} V(\mathbf{r}_i - \mathbf{r}_j) \left| \langle c_{i s}^\dagger c_{j s} \rangle - \langle c_{i s}^\dagger c_{j s} \rangle_0 \right|^2 \\ &\quad + U \sum_{\mathbf{r}_i} \left(\langle c_{i \uparrow}^\dagger c_{i \uparrow} \rangle - \langle c_{i \uparrow}^\dagger c_{i \uparrow} \rangle_0 \right) \left(\langle c_{i \downarrow}^\dagger c_{i \downarrow} \rangle - \langle c_{i \downarrow}^\dagger c_{i \downarrow} \rangle_0 \right) + \sum_{\mathbf{r}_i, \mathbf{r}_j, s} t(\mathbf{r}_i - \mathbf{r}_j) e^{i\theta_{i,j}} \langle c_{i s}^\dagger c_{j s} \rangle. \end{aligned} \quad (\text{D5})$$

The Coulomb interaction is split into the Hartree or direct and Fock or exchange terms, with the plus and minus signs in front respectively. In our algorithm, we always work with the Fock matrix $\langle c_{i s}^\dagger c_{i s} \rangle - \langle c_{i s}^\dagger c_{i s} \rangle_0$, so the values reported for the kinetic energy have a constant offset of $\sum_{\mathbf{r}_i, \mathbf{r}_j, s} t(\mathbf{r}_i - \mathbf{r}_j) e^{i\theta_{i,j}} \langle c_{i s}^\dagger c_{j s} \rangle_0$.

Appendix E: Additional Hartree-Fock results

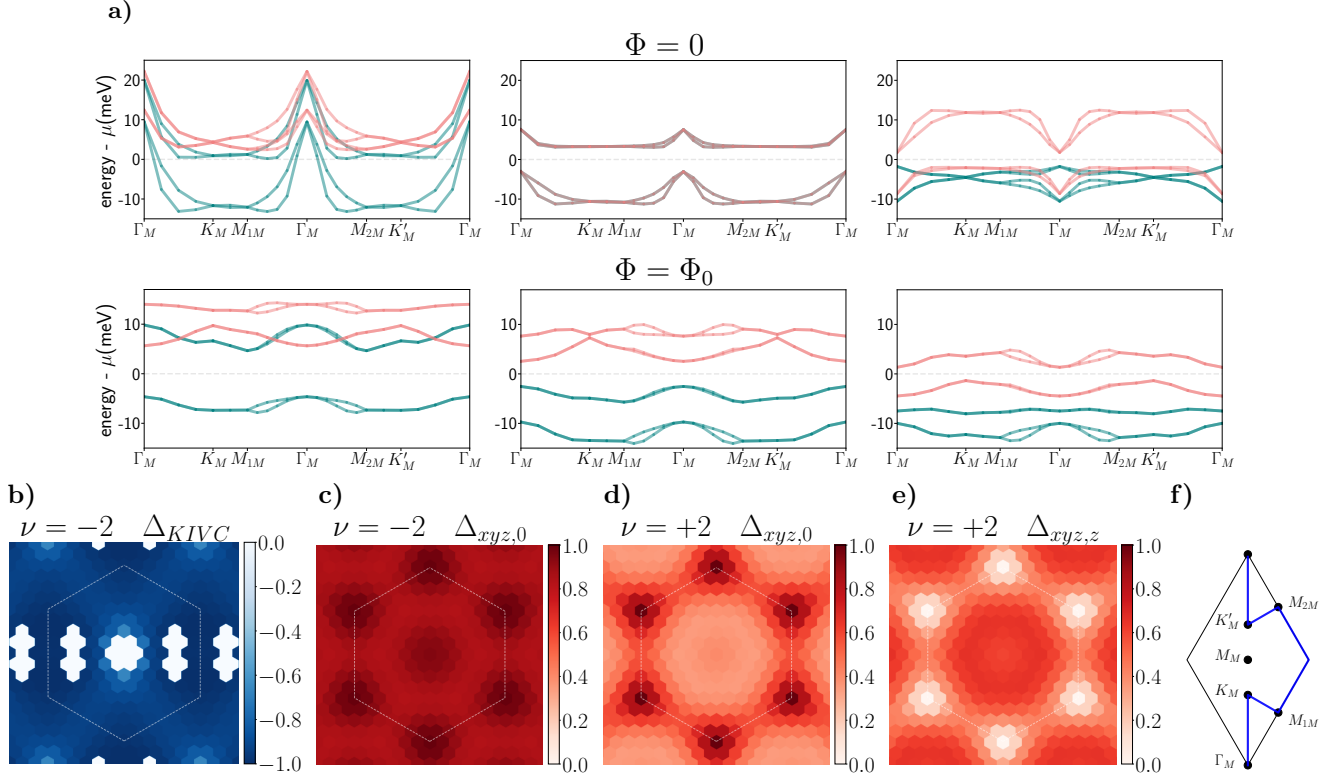


FIG. E.4: **Hartree-Fock results for $\epsilon = 30$, $U = 4$ eV.** **a)** The KIVC band structures, for $\Phi = 0$, and the ground state bands, for Φ_0 . Spin up bands are in blue and spin down bands in red. From left to right the doping levels are $\nu = -2, 0, +2$. The critical value for the SP-KIVC transition is found to be $U_c = 1.1$ eV. In **b)** we show Δ_{KIVC} for $\nu = -2$ at zero flux. There is a hole pocket around Γ_M and two electron pockets at its sides, where the order parameter is ill-defined. In Fig. 8b) the extra electrons come from the opposite spin, so the electron pockets are not visible. In this phase C_{3z} is broken but C_{2z} and C_{2x} are preserved. C_{3z} breaking is not evident in the plot of a) because the C_{3z} (or C_{6z}) related lines are related by C_{2x} (or $C_{2y} = C_{2z}C_{2x}$) also. In **c)** we plot $\Delta_{xyz,0}$ of the hole doped state under one flux quantum, and in **d)** and **e)** the two dominant order parameters for the state at $\nu = +2$ and Φ_0 flux. Unlike for $\epsilon = 10$, $U = 4$ eV, both parameters contribute equitably. The phase transition to the IVC state takes place at some value of ϵ between 30 and 50. **f)** The path of the band structure plots.

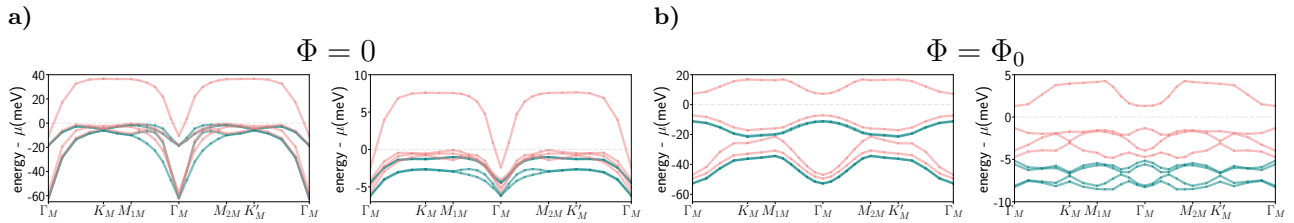


FIG. E.5: **Correlated insulators at $\nu = +3$.** **a)** Chern insulators with Chern number 1 that have been reported in samples with explicit C_{2z} breaking due to the substrate[24, 25]. We obtain incipient valley polarized anomalous Hall states without the need for C_{2z} breaking at zero field, both for $\epsilon = 10$, $U = 4$ eV, plotted to the left, and $\epsilon = 50$, $U = 4$ eV to the right. **b)** Gapped insulators at $B = 26.5$ T. In both cases we get valley polarized states with Chern number +1. Interestingly, the band structures are very dissimilar for $\epsilon = 10$, $U = 4$ eV plotted to the left, and $\epsilon = 50$, $U = 4$ eV to the right.

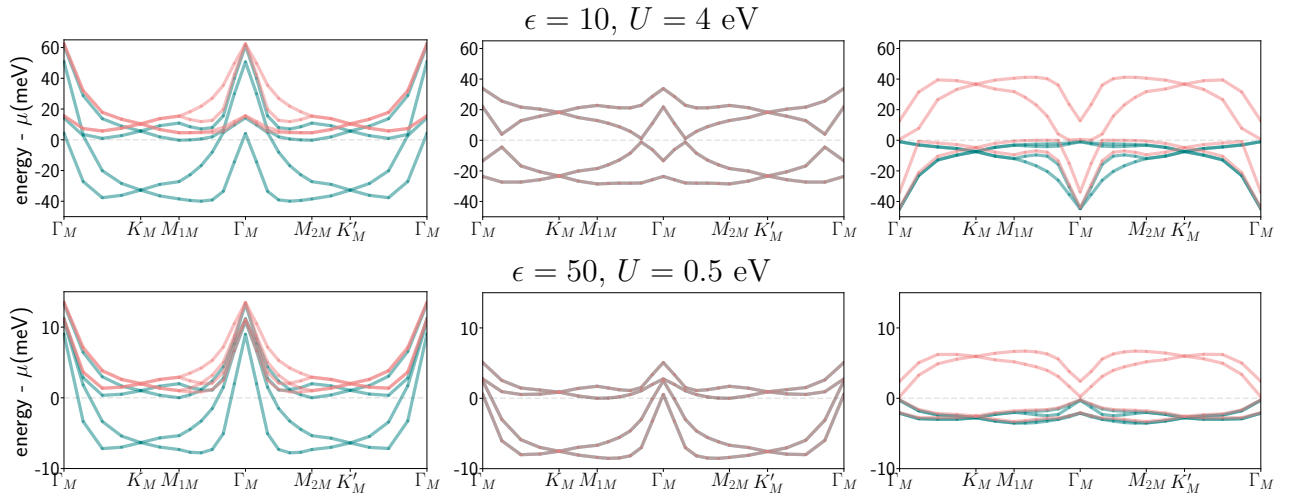


FIG. E.6: **The self-consistent valley polarized states.** Spin up bands are shown in blue and spin down bands in red. From left to right the doping levels are $\nu = -2, 0, +2$. The order parameter is the valley polarization $\langle \sigma_0 \tau_z \rangle$ predominantly. Only for $\epsilon = 10, U = 4 \text{ eV}$ the inter-Chern parameter appears around Γ_M .

Appendix F: Tables with the energies of the candidate and self-consistent states

$\nu = -2, \xi = 10 \text{ nm}, \Phi = \Phi_0$						
state	wave function	kinetic	$\epsilon \times \text{Hartree}$	$\epsilon \times \text{Fock}$	$\epsilon \times \text{Coulomb}$	Hubbard/ U
IVC	$\prod_{\mathbf{k}} \prod_{\lambda} \frac{1}{\sqrt{2}} (d_{\mathbf{k}K\lambda\uparrow}^\dagger + id_{\mathbf{k}K'\lambda\uparrow}^\dagger) 0\rangle$	-48144.42	328.32	-38862.09	-38533.77	11.52
VP	$\prod_{\mathbf{k}} d_{\mathbf{k}K+1\uparrow}^\dagger d_{\mathbf{k}K-1\uparrow}^\dagger 0\rangle$	-48144.42	327.78	-38861.38	-38533.60	11.52
non int. GS	-	-48150.18	225.32	-38753.07	-38527.76	11.37
$\nu = -2, \xi = 20 \text{ nm}, \Phi = \Phi_0$						
state	wave function	kinetic	$\epsilon \times \text{Hartree}$	$\epsilon \times \text{Fock}$	$\epsilon \times \text{Coulomb}$	Hubbard/ U
IVC	$\prod_{\mathbf{k}} \prod_{\lambda} \frac{1}{\sqrt{2}} (d_{\mathbf{k}K\lambda\uparrow}^\dagger + id_{\mathbf{k}K'\lambda\uparrow}^\dagger) 0\rangle$	-48144.42	919.39	-40665.49	-39746.10	11.52
VP	$\prod_{\mathbf{k}} d_{\mathbf{k}K+1\uparrow}^\dagger d_{\mathbf{k}K-1\uparrow}^\dagger 0\rangle$	-48144.42	918.85	-40664.80	-39745.95	11.52
non int. GS	-	-48150.18	816.56	-40547.45	-39730.89	11.37
$\nu = 0, \xi = 10 \text{ nm}, \Phi = \Phi_0$						
state	wave function	kinetic	$\epsilon \times \text{Hartree}$	$\epsilon \times \text{Fock}$	$\epsilon \times \text{Coulomb}$	Hubbard/ U
IVC	$\prod_{\mathbf{k}} \prod_{s\lambda} \frac{1}{\sqrt{2}} (d_{\mathbf{k}K\lambda s}^\dagger + id_{\mathbf{k}K'\lambda s}^\dagger) 0\rangle$	-46554.33	-343.05	-38855.98	-39199.03	11.45
VP	$\prod_{\mathbf{k}} \prod_s d_{\mathbf{k}K+1s}^\dagger d_{\mathbf{k}K-1s}^\dagger 0\rangle$	-46554.33	-345.21	-38854.56	-39199.77	11.52
VSP	$\prod_{\mathbf{k}} d_{\mathbf{k}K+1\uparrow}^\dagger d_{\mathbf{k}K-1\uparrow}^\dagger d_{\mathbf{k}K'+1\downarrow}^\dagger d_{\mathbf{k}K'-1\downarrow}^\dagger 0\rangle$	-46554.33	-342.64	-38854.56	-39197.20	11.33
SP	$\prod_{\mathbf{k}} \prod_{\eta\lambda} d_{\mathbf{k}\eta\lambda\uparrow}^\dagger 0\rangle$	-46554.33	-342.64	-38849.33	-39191.97	10.75
non int. GS	-	-46565.86	8.86	-38637.94	-38629.08	11.77
$\nu = 0, \xi = 20 \text{ nm}, \Phi = \Phi_0$						
state	wave function	kinetic	$\epsilon \times \text{Hartree}$	$\epsilon \times \text{Fock}$	$\epsilon \times \text{Coulomb}$	Hubbard/ U
IVC	$\prod_{\mathbf{k}} \prod_{s\lambda} \frac{1}{\sqrt{2}} (d_{\mathbf{k}K\lambda s}^\dagger + id_{\mathbf{k}K'\lambda s}^\dagger) 0\rangle$	-46554.33	-346.62	-40657.36	-41003.99	11.45
VP	$\prod_{\mathbf{k}} \prod_s d_{\mathbf{k}K+1s}^\dagger d_{\mathbf{k}K-1s}^\dagger 0\rangle$	-46554.34	-348.80	-40655.99	-41004.79	11.52
VSP	$\prod_{\mathbf{k}} d_{\mathbf{k}K+1\uparrow}^\dagger d_{\mathbf{k}K-1\uparrow}^\dagger d_{\mathbf{k}K'+1\downarrow}^\dagger d_{\mathbf{k}K'-1\downarrow}^\dagger 0\rangle$	-46554.33	-346.21	-40655.99	-41002.20	11.33
SP	$\prod_{\mathbf{k}} \prod_{\eta\lambda} d_{\mathbf{k}\eta\lambda\uparrow}^\dagger 0\rangle$	-46554.33	-346.21	-40650.70	-40996.92	10.75
non int. GS	-	-46565.86	4.22	-40421.29	-40417.07	11.77
$\nu = +2, \xi = 10 \text{ nm}, \Phi = \Phi_0$						
state	wave function	kinetic	$\epsilon \times \text{Hartree}$	$\epsilon \times \text{Fock}$	$\epsilon \times \text{Coulomb}$	Hubbard/ U
IVC	$\prod_{\mathbf{k}} \prod_{\lambda} \frac{1}{\sqrt{2}} (d_{\mathbf{k}K\lambda\downarrow} + id_{\mathbf{k}K'\lambda\downarrow}) +4\rangle$	-44964.25	474.60	-38843.22	-38368.62	11.34
VP	$\prod_{\mathbf{k}} d_{\mathbf{k}K+1\downarrow} d_{\mathbf{k}K-1\downarrow} +4\rangle$	-44964.25	474.05	-38842.51	-38368.45	11.34
non int. GS	-	-44971.37	821.80	-38664.38	-37842.58	11.73
$\nu = +2, \xi = 20 \text{ nm}, \Phi = \Phi_0$						
state	wave function	kinetic	$\epsilon \times \text{Hartree}$	$\epsilon \times \text{Fock}$	$\epsilon \times \text{Coulomb}$	Hubbard/ U
IVC	$\prod_{\mathbf{k}} \prod_{\lambda} \frac{1}{\sqrt{2}} (d_{\mathbf{k}K\lambda\downarrow} + id_{\mathbf{k}K'\lambda\downarrow}) +4\rangle$	-44964.25	1065.69	-40642.57	-39576.89	11.34
VP	$\prod_{\mathbf{k}} d_{\mathbf{k}K+1\downarrow} d_{\mathbf{k}K-1\downarrow} +4\rangle$	-44964.25	1065.14	-40641.89	-39576.74	11.34
non int. GS	-	-44971.37	1412.04	-40439.88	-39027.84	11.73

TABLE F1: Expectation values of the energy of candidates states for the correlated insulators of MATBG at one magnetic flux quantum. We list the states for fillings $\nu = 0, \pm 2$ setting ξ to 10 and 20 nm. The values are in units of meV per unit cell, and U is given in eV. The state non int. GS is the ground state of the non interacting system. Coincidentally the kinetic ground state at hole doping is given by the filled valence band of the spin \uparrow , and at charge neutrality by the valence bands of both spins, as can be seen in Fig. 3. $|0\rangle$ denotes the state with filled remote bands and $|+4\rangle$ the $\nu = +4$ insulator. The Zeeman energy is ± 1.535 meV per electron and is not explicitly included.

$\nu = -2, \xi = 10 \text{ nm}, \Phi = 0$						
state	wave function	kinetic	$\epsilon \times \text{Hartree}$	$\epsilon \times \text{Fock}$	$\epsilon \times \text{Coulomb}$	Hubbard/ U
KIVC	$\prod_{\mathbf{k}} \frac{1}{2} (d_{\mathbf{k}K A \uparrow}^\dagger + d_{\mathbf{k}K' B \uparrow}^\dagger) (d_{\mathbf{k}K B \uparrow}^\dagger - d_{\mathbf{k}K' A \uparrow}^\dagger) 0\rangle$	-47981.11	642.52	-38976.71	-38334.19	12.07
VP	$\prod_{\mathbf{k}} d_{\mathbf{k}K A \uparrow}^\dagger d_{\mathbf{k}K B \uparrow}^\dagger 0\rangle$	-47981.11	642.52	-38975.58	-38333.06	12.07
TIVC	$\prod_{\mathbf{k}} \frac{1}{2} (d_{\mathbf{k}K A \uparrow}^\dagger + d_{\mathbf{k}K' B \uparrow}^\dagger) (d_{\mathbf{k}K B \uparrow}^\dagger + d_{\mathbf{k}K' A \uparrow}^\dagger) 0\rangle$	-47981.11	641.62	-38966.78	-38325.16	12.07
QAH-IVC	$\prod_{\mathbf{k}} \prod_s \frac{1}{\sqrt{2}} (d_{\mathbf{k}K A_s}^\dagger + d_{\mathbf{k}K' B_s}^\dagger) 0\rangle$	-47981.11	641.62	-38969.92	-38328.30	12.41
QAH-VP	$\prod_{\mathbf{k}} \prod_s d_{\mathbf{k}K A_s}^\dagger 0\rangle$	-47981.11	637.34	-38967.80	-38330.46	12.53
VH	$\prod_{\mathbf{k}} d_{\mathbf{k}K A \uparrow}^\dagger d_{\mathbf{k}K' A \uparrow}^\dagger 0\rangle$	-47981.11	637.34	-38963.67	-38326.34	12.07
non int. GS	-	-47982.83	581.99	-38598.70	-38016.71	12.34
$\nu = -2, \xi = 20 \text{ nm}, \Phi = 0$						
state	wave function	kinetic	$\epsilon \times \text{Hartree}$	$\epsilon \times \text{Fock}$	$\epsilon \times \text{Coulomb}$	Hubbard/ U
KIVC	$\prod_{\mathbf{k}} \frac{1}{2} (d_{\mathbf{k}K A \uparrow}^\dagger + d_{\mathbf{k}K' B \uparrow}^\dagger) (d_{\mathbf{k}K B \uparrow}^\dagger - d_{\mathbf{k}K' A \uparrow}^\dagger) 0\rangle$	-47981.11	1232.78	-40791.19	-39558.42	12.07
VP	$\prod_{\mathbf{k}} d_{\mathbf{k}K A \uparrow}^\dagger d_{\mathbf{k}K B \uparrow}^\dagger 0\rangle$	-47981.11	1232.78	-40790.08	-39557.30	12.07
TIVC	$\prod_{\mathbf{k}} \frac{1}{2} (d_{\mathbf{k}K A \uparrow}^\dagger + d_{\mathbf{k}K' B \uparrow}^\dagger) (d_{\mathbf{k}K B \uparrow}^\dagger + d_{\mathbf{k}K' A \uparrow}^\dagger) 0\rangle$	-47981.11	1231.88	-40780.57	-39548.70	12.07
QAH-IVC	$\prod_{\mathbf{k}} \prod_s \frac{1}{\sqrt{2}} (d_{\mathbf{k}K A_s}^\dagger + d_{\mathbf{k}K' B_s}^\dagger) 0\rangle$	-47981.11	1231.88	-40783.73	-39551.85	12.41
QAH-VP	$\prod_{\mathbf{k}} \prod_s d_{\mathbf{k}K A_s}^\dagger 0\rangle$	-47981.11	1227.56	-40781.60	-39554.04	12.53
VH	$\prod_{\mathbf{k}} d_{\mathbf{k}K A \uparrow}^\dagger d_{\mathbf{k}K' A \uparrow}^\dagger 0\rangle$	-47981.11	1227.56	-40777.43	-39549.87	12.07
non int. GS	-	-47982.83	1172.38	-40353.58	-39181.20	12.34
$\nu = 0, \xi = 10 \text{ nm}, \Phi = 0$						
state	wave function	kinetic	$\epsilon \times \text{Hartree}$	$\epsilon \times \text{Fock}$	$\epsilon \times \text{Coulomb}$	Hubbard/ U
KIVC	$\prod_{\mathbf{k}} \prod_s \frac{1}{2} (d_{\mathbf{k}K A_s}^\dagger + d_{\mathbf{k}K' B_s}^\dagger) (d_{\mathbf{k}K B_s}^\dagger - d_{\mathbf{k}K' A_s}^\dagger) 0\rangle$	-46395.22	-364.23	-38971.96	-39336.20	11.98
VP	$\prod_{\mathbf{k}} \prod_s d_{\mathbf{k}K A_s}^\dagger d_{\mathbf{k}K B_s}^\dagger 0\rangle$	-46395.22	-364.23	-38969.71	-39333.94	11.98
TIVC	$\prod_{\mathbf{k}} \prod_s \frac{1}{2} (d_{\mathbf{k}K A \uparrow}^\dagger + d_{\mathbf{k}K' B \uparrow}^\dagger) (d_{\mathbf{k}K B \uparrow}^\dagger + d_{\mathbf{k}K' A \uparrow}^\dagger) 0\rangle$	-46395.22	-367.82	-38952.11	-39319.93	12.18
SP	$\prod_{\mathbf{k}} \prod_{\eta\sigma} d_{\mathbf{k}\eta\sigma\uparrow}^\dagger 0\rangle$	-46395.22	-364.23	-38959.38	-39323.62	10.81
VH	$\prod_{\mathbf{k}} \prod_s d_{\mathbf{k}K A_s}^\dagger d_{\mathbf{k}K' A_s}^\dagger 0\rangle$	-46395.22	-384.95	-38945.89	-39330.85	12.67
non int. GS	-	-46398.20	-364.92	-38439.73	-38804.65	12.00
$\nu = 0, \xi = 20 \text{ nm}, \Phi = 0$						
state	wave function	kinetic	$\epsilon \times \text{Hartree}$	$\epsilon \times \text{Fock}$	$\epsilon \times \text{Coulomb}$	Hubbard/ U
KIVC	$\prod_{\mathbf{k}} \prod_s \frac{1}{2} (d_{\mathbf{k}K A_s}^\dagger + d_{\mathbf{k}K' B_s}^\dagger) (d_{\mathbf{k}K B_s}^\dagger - d_{\mathbf{k}K' A_s}^\dagger) 0\rangle$	-46395.22	-368.00	-40784.72	-41152.72	11.98
VP	$\prod_{\mathbf{k}} \prod_s d_{\mathbf{k}K A_s}^\dagger d_{\mathbf{k}K B_s}^\dagger 0\rangle$	-46395.22	-368.00	-40782.49	-41150.49	11.98
TIVC	$\prod_{\mathbf{k}} \prod_s \frac{1}{2} (d_{\mathbf{k}K A \uparrow}^\dagger + d_{\mathbf{k}K' B \uparrow}^\dagger) (d_{\mathbf{k}K B \uparrow}^\dagger + d_{\mathbf{k}K' A \uparrow}^\dagger) 0\rangle$	-46395.22	-371.62	-40763.47	-41135.10	12.18
SP	$\prod_{\mathbf{k}} \prod_{\eta\sigma} d_{\mathbf{k}\eta\sigma\uparrow}^\dagger 0\rangle$	-46395.22	-368.00	-40772.06	-41140.16	10.81
VH	$\prod_{\mathbf{k}} \prod_s d_{\mathbf{k}K A_s}^\dagger d_{\mathbf{k}K' A_s}^\dagger 0\rangle$	-46395.22	-388.88	-40757.19	-41146.07	12.67
non int. GS	-	-46398.20	-368.72	-40176.25	-40545.97	12.00
$\nu = +2, \xi = 10 \text{ nm}, \Phi = 0$						
state	wave function	kinetic	$\epsilon \times \text{Hartree}$	$\epsilon \times \text{Fock}$	$\epsilon \times \text{Coulomb}$	Hubbard/ U
KIVC	$\prod_{\mathbf{k}} \frac{1}{2} (d_{\mathbf{k}K A \uparrow} + d_{\mathbf{k}K' B \uparrow}) (d_{\mathbf{k}K B \uparrow} - d_{\mathbf{k}K' A \uparrow}) +4\rangle$	-44809.34	543.00	-38954.64	-38411.64	11.88
VP	$\prod_{\mathbf{k}} d_{\mathbf{k}K A \uparrow} d_{\mathbf{k}K B \uparrow} +4\rangle$	-44809.34	543.00	-38953.51	-38410.51	11.88
TIVC	$\prod_{\mathbf{k}} \frac{1}{2} (d_{\mathbf{k}K A \uparrow} + d_{\mathbf{k}K' B \uparrow}) (d_{\mathbf{k}K B \uparrow} + d_{\mathbf{k}K' A \uparrow}) +4\rangle$	-44809.34	542.11	-38944.71	-38402.61	11.88
QAH-IVC	$\prod_{\mathbf{k}} \prod_s \frac{1}{\sqrt{2}} (d_{\mathbf{k}K A_s} + d_{\mathbf{k}K' B_s}) +4\rangle$	-44809.34	542.11	-38947.85	-38405.74	12.22
QAH-VP	$\prod_{\mathbf{k}} \prod_s d_{\mathbf{k}K A_s} +4\rangle$	-44809.34	537.82	-38945.73	-38407.91	12.35
VH	$\prod_{\mathbf{k}} d_{\mathbf{k}K A \uparrow} d_{\mathbf{k}K' A \uparrow} +4\rangle$	-44809.34	537.82	-38941.61	-38403.78	11.88
non int. GS	-	-44812.85	683.22	-38576.60	-37893.38	12.29
$\nu = +2, \xi = 20 \text{ nm}, \Phi = 0$						
state	wave function	kinetic	$\epsilon \times \text{Hartree}$	$\epsilon \times \text{Fock}$	$\epsilon \times \text{Coulomb}$	Hubbard/ U
KIVC	$\prod_{\mathbf{k}} \frac{1}{2} (d_{\mathbf{k}K A \uparrow} + d_{\mathbf{k}K' B \uparrow}) (d_{\mathbf{k}K B \uparrow} - d_{\mathbf{k}K' A \uparrow}) +4\rangle$	-44809.34	1133.46	-40765.58	-39632.12	11.88
VP	$\prod_{\mathbf{k}} d_{\mathbf{k}K A \uparrow} d_{\mathbf{k}K B \uparrow} +4\rangle$	-44809.34	1133.46	-40764.47	-39631.01	11.88
TIVC	$\prod_{\mathbf{k}} \frac{1}{2} (d_{\mathbf{k}K A \uparrow} + d_{\mathbf{k}K' B \uparrow}) (d_{\mathbf{k}K B \uparrow} + d_{\mathbf{k}K' A \uparrow}) +4\rangle$	-44809.34	1132.55	-40754.96	-39622.41	11.88
QAH-IVC	$\prod_{\mathbf{k}} \prod_s \frac{1}{\sqrt{2}} (d_{\mathbf{k}K A_s} + d_{\mathbf{k}K' B_s}) +4\rangle$	-44809.34	1132.55	-40758.11	-39625.56	12.22
QAH-VP	$\prod_{\mathbf{k}} \prod_s d_{\mathbf{k}K A_s} +4\rangle$	-44809.34	1128.23	-40755.98	-39627.75	12.35
VH	$\prod_{\mathbf{k}} d_{\mathbf{k}K A \uparrow} d_{\mathbf{k}K' A \uparrow} +4\rangle$	-44809.34	1128.23	-40751.81	-39623.58	11.88
non int. GS	-	-44812.85	1273.27	-4032.06	-39058.79	12.29

TABLE F2: Expectation values of the energy of candidates states for the correlated insulators of MATBG at zero magnetic field. We list the states for fillings $\nu = -2, 0, +2$ setting ξ to 10 and 20 nm. The energies are in units of meV per unit cell, and the value of U is given in eV. The state non int. GS is the ground state of the non interacting system. QAH (Quantum anomalous Hall) states have Chern number 2 and are stabilized by small out of plane magnetic fields[8, 9]. $|0\rangle$ denotes the state with the filled remote bands and $|+4\rangle$ the $\nu = +4$ insulator.

$\nu, (\epsilon, U)$	kinetic	$\epsilon \times \text{Hartree}$	$\epsilon \times \text{Fock}$	$\epsilon \times \text{Coulomb}$	Hubbard/ U
-2, (10, 4 eV)	-48147.31	228.05	-38903.47	-38675.42	11.39
-2, (50, 0.5 eV)	-48149.36	222.52	-38842.95	-38620.43	11.37
0, (10, 4 eV)	-46552.57	-340.91	-38890.94	-39231.85	10.90
0, (50, 0.5 eV)	-46554.48	-341.91	-38845.54	-39187.45	10.76
+2, (10, 4 eV)	-44959.04	319.40	-38846.62	-38527.22	11.08
+2, (50, 0.5 eV)	-44964.44	476.25	-38852.51	-38376.26	11.34

TABLE F3: **Expectation values of the energy of the ground states for $B = 26.5$ T.** The fillings are $\nu = 0, \pm 2$ and the interaction parameters $\epsilon = 10, U = 4$ eV and $\epsilon = 10, U = 0.5$ eV. The gate distance is set to $\xi = 10$ nm. The values are in units of meV per unit cell, and U is given in eV. The Zeeman energy is ± 1.535 meV per electron and is not explicitly included.

$\nu = -2, \epsilon = 10, U = 4$ eV					
order	kinetic	$\epsilon \times \text{Hartree}$	$\epsilon \times \text{Fock}$	$\epsilon \times \text{Coulomb}$	Hubbard/ U
KIVC	-47980.57	631.44	-39002.21	-38370.76	12.07
VP	-47981.24	613.44	-38958.61	-38345.17	12.05
$\nu = -2, \epsilon = 50, U = 0.5$ eV					
order	kinetic	$\epsilon \times \text{Hartree}$	$\epsilon \times \text{Fock}$	$\epsilon \times \text{Coulomb}$	Hubbard/ U
KIVC	-47981.42	602.60	-38951.76	-38349.17	12.12
VP	-47981.58	600.96	-38936.46	-38335.50	12.03
$\nu = 0, \epsilon = 10, U = 4$ eV					
order	kinetic	$\epsilon \times \text{Hartree}$	$\epsilon \times \text{Fock}$	$\epsilon \times \text{Coulomb}$	Hubbard/ U
KIVC	-46393.94	-364.72	-39036.56	-39401.29	11.99
SP	-46394.61	-364.36	-38980.15	-39344.50	10.88
VP	-46394.61	-364.36	-38989.93	-39354.29	11.98
$\nu = 0, \epsilon = 50, U = 0.5$ eV					
order	kinetic	$\epsilon \times \text{Hartree}$	$\epsilon \times \text{Fock}$	$\epsilon \times \text{Coulomb}$	Hubbard/ U
KIVC	-46394.82	-365.14	-39003.10	-39368.25	11.98
SP	-46395.38	-364.90	-38953.35	-39318.25	10.84
VP	-46395.38	-364.90	-38963.48	-39328.38	11.98
$\nu = +2, \epsilon = 10, U = 4$ eV					
order	kinetic	$\epsilon \times \text{Hartree}$	$\epsilon \times \text{Fock}$	$\epsilon \times \text{Coulomb}$	Hubbard/ U
KIVC	-44808.71	545.40	-38986.29	-38440.89	11.89
VP	-44809.02	541.18	-38961.14	-38419.95	11.88
$\nu = +2, \epsilon = 50, U = 0.5$ eV					
order	kinetic	$\epsilon \times \text{Hartree}$	$\epsilon \times \text{Fock}$	$\epsilon \times \text{Coulomb}$	Hubbard/ U
KIVC	-44809.07	544.39	-38973.52	-38429.13	11.89
VP	-44809.34	543.00	-38953.51	-38410.51	11.88

TABLE F4: **Expectation values of the energy of the self-consistent states for $B = 0$ T.** The fillings are $\nu = 0, \pm 2$ and the interaction parameters $\epsilon = 10, U = 4$ eV and $\epsilon = 10, U = 0.5$ eV. The gate distance is set to $\xi = 10$ nm. The states are labeled by the dominant order parameter. The values are in units of meV per unit cell, and U is given in eV.